Mica trace-element signatures: Highlighting superimposed W-Sn mineralizations and fluid sources

Loïs Monnier, Stefano Salvi, Jérémie Melleton, Philippe Lach, Anthony Pochon, Laurent Bailly, Didier Béziat, Philippe de Parseval

Mica trace-element signatures: Highlighting superimposed W-Sn mineralizations and fluid sources

Loïs Monnier, Stefano Salvi, Jérémie Melleton, Philippe Lach, Anthony Pochon, Laurent Bailly, Didier Béziat, Philippe de Parseval

Mica trace-element signatures: highlighting superimposed W - Sn mineralizations and fluid sources

Loïs Monnier[1,*], Stefano Salvi[1], Jérémie Melleton[2], Philippe Lach[2], Anthony Pochon[3], Laurent Bailly[2], Didier Béziat[1], Philippe De Parseval[1].

1 GET, CNRS/IRD/UPS/CNES, Toulouse University, 14 avenue Edouard Belin, 31400 Toulouse, France

2 BRGM, 3 Avenue Claude Guillemin, 45000 Orléans, France

3 ISTO, CNRS/BRGM, Orléans University, 1A rue de la Férollerie, 45000 Orléans, France

** corresponding author, loismonnier@yahoo.fr*

Highlights

- Mica generations are characterized by unique trace-element signatures.
- Igneous lepidolite is the main host of W in the Beauvoir granite body.
- Alteration of igneous micas can lead to economic W deposition.
- Greisen micas can incorporate significant Sn, inhibiting cassiterite deposition.

Abstract

In the Echassières district of the French Massif Central, occur several outstanding magmatic/hydrothermal systems enriched in strategic metals, such as the Beauvoir rare-metal granite. In this contribution we propose a systematic approach, based on mica trace chemistry, to decipher the different events leading to mineralization. Twelve groups of micas were defined by their specific petrographic features and/or location in the district. Their trace element composition, obtained by LA-ICP-MS, varies widely from one mica group to another, although homogeneous signatures within groups could be distinguished. Some of the trace elements are remarkably enriched, such as W in igneous lepidolite and Sn in greisen muscovite, both of which occur in the Beauvoir granite. A statistical approach based on a set of multivariate analyses highlights that the trace chemistry of micas is inherited from their source, whether hydrothermal or igneous, thus providing a signature for their origin. This approach also shows that differences in major element

composition (i.e., different mica species) impact only slightly the trace-element signature. For instance, muscovite and zinnwaldite from one granite have a coherent signature, but they contrast with same mica species in another granite or hydrothermal veins. It is thus possible to genetically link two different mica species from remote locations, or inversely, to recognize different origins for a same mica species in the same sample (e.g., superposed alterations). A second, important implication is that trace-element signatures of micas provide a record of metal remobilization and transport. In the Echassières district, greisen alteration of the Beauvoir granite caused dissolution of W-rich (ca. 290 ppm in average) lepidolite and cassiterite (SnO_2). Newly-formed greisen muscovite incorporated most remobilized Sn (ca. 1000 ppm in average), while W precipitated in distal quartz veins as wolframite. As a consequence, Sn is concentrated in the granite, while W occurs outside of it. This is also indicated by the gradual Sn decrease and W increase recorded in micas from distal veins. Finally, wolframite-bearing veins do not contain cassiterite, validating mica trace-element chemistry as a powerful tool to decipher Sn-W ore forming hydrothermal processes.

Keywords

Micas, trace-element signature, LA-ICP-MS, Beauvoir granite, Echassières district.

1. Introduction

Minerals of the mica group can incorporate a wide variety of elements due to their sheet structure and countless substitutions permitted by complex multiple solid solutions (Foster, 1960; Hazen and Wones, 1972; Iiyama and Volfinger, 1976; see also Brigatti et al., 2002 and references therein). Evolved granitic systems and related hydrothermal assemblages commonly display complex parageneses that include a variety of mica species (more or less rich in F, Li, Rb, Cs, Fe, Mg; Tischendorf et al., 2001). These micas can exhibit a remarkable enrichment in incompatible elements, to the point that they are considered important reservoirs of incompatible LILE (Large Ion Lithophile Elements) in various rocks (Beswick, 1973; Nash and Crecraft, 1985; Adam and Green, 2006; Bebout, et al., 2007; Hulsbosch et al., 2014). Moreover, it has recently been shown that micas are good competitors for the HFSE (High Field-Strength Elements; also highly incompatible) against element-specific accessory phases (e.g., see Zhu et al., 2018 and Yang et al., 2020, for Nb-Ta and **Breiter et al.,** Guimarães et al., 2021, for Sn). Consequently, crystallization (or inversely, dissolution) of a specific mica generation during hydrothermal alteration can drastically affect the fate of these metals and the potential for mineralization.

In granitic systems, W mineralization is usually related to acidic alteration zones (e.g., greisen in peraluminous granites, sericitization in porphyries) that are rich in micas. Because of this, a growing number of researchers are turning to the study of the trace composition of mica from Sn-W mineralized systems (e.g., Li et al., 2015, 2018; Xie et al., 2015, 2019; Legros et al., 2016, 2018; Breiter et al., 2017, 2019; Gao et al., 2019; Sun et al., 2019; Yin et al., 2019; Azadbakht and Lentz, 2020; Azadbakht et al., 2020; Chen et al., 2020; Xie et al., 2020; Wei et al., 2020; Codeço et al., 2021; **Duan et al., 2021;** Guimarães et al., 2021; Shi et al., 2021; Li et al., 2021). An interesting outcome of these studies is that most micas have much higher W, Sn and Nb-Ta contents than micas in barren magmatic-hydrothermal systems. However, it is also reported that several trace elements common in these micas can vary by few orders of magnitude in the different deposits (Breiter et al., 2017; Codeço et al., 2021; Wei et al., 2020), and even within a single deposit (e.g., Legros et al., 2018; Breiter et al., 2019). As a consequence, these studies contain as many

64 specific trace-element signatures as there are analyzed mica generations. To enhance our knowledge on
65 the potential applications of trace element distribution in micas, we investigate the Echassières

district (France), a particularly complex system that provides a unique opportunity to monitor the evolution of mica composition across a protracted ore depositing event, characterized by several mineralizing episodes.

2. Geological settings

The Echassières district (Fig.1.A) is a long-lived polymetallic (Li, W, Sn, Nb-Ta, Sb) deposit located in the Sioule nappe of the northern French Massif Central. The architecture of the Echassières district consists of an antiform where three metasedimentary units are stacked, intruded in their core by the Colettes two-micas granite and to the south by the smaller Beauvoir rare-metal granite. The bulk of the mineralization is restricted to within a radius of 3 km around the Beauvoir granite (Fig.1.B). Ore deposition took place during different stages of the Variscan belt evolution, likely ranging from subduction and arc magmatism (>360 Ma) to phases of orogenic collapse (310 Ma; Monnier et al., 2021a). The peak of the Barrovian metamorphism in the Sioule nappe occurred at 350-360 Ma (Do Couto et al., 2016), with temperature and pressure estimated at ca. 600 °C and 7 kb for the lower unit of the antiform (Schulz, 2009).

At least three generations of wolframite (Monnier et al., 2019, 2020) and two generations of stibnite (Monnier et al., 2021b) occur in the Sioule nappe. Some of these mineralizations were mined in the 20th century (Mazet and La Bosse localities for the wolframite and Nades for the stibnite; Aubert and Contamine, 1958; Aubert, 1969), while columbo-tantalite is presently recovered as by-product of kaolinite extraction at the Beauvoir granite quarry. Intrusion of Beauvoir/Colettes complex was the most recent, and consequently the best preserved magmatic/hydrothermal event in the zone. The Beauvoir rare metal granite (RMG) has been intensively investigated in the past by a number of authors (Fouillac and Rossi, 1991; Cuney et al., 1992, Raimbault et al., 1995), who concord to evoke extreme fractionation processes coupled to massive meteoric fluid incorporation to explain the outstanding enrichment of incompatible elements at the magmatic stage. More recently, the hydrothermal events were investigated in depth to unravel the several alteration episodes superimposed in the host schist. Stockwork quartz veins (>360 Ma) and topaz veins (ca. 335 Ma) were recognized as distinct igneous-related hydrothermal episodes that took place well before crystallization of the Beauvoir granite (ca. 310 Ma; Harlaux et al., 2017; Monnier et al.,

2019, 2020). Three alteration episodes affected the Beauvoir granite and surrounding rocks, to variable extent. An early orthomagmatic stage, initiated by exsolution of a hot (> 450 °C) fluid during granite crystallization, induced acidic F-rich and alkali alterations, which are manifested mostly in contact zones between the granite and the host rock (Cuney et al., 1992; Monnier et al., 2020). A second stage is characterized by widespread greisenization (Monnier et al., 2018; Monnier et al., 2020). Key features of the greisen fluid include F-poor and P-rich sericitization, marked by the occurrence of abundant OH-muscovite and apatite (Monnier et al., 2019). Greisen alteration was a continuous process, initiated within the granite at ca. 450°C and evolving towards the host rock where it waned at about 200°C. Peak greisen activity in the granite was contemporaneous to fracturing episodes in the area, promoting formation of proximal veins around the granitic system, by percolation of the Beauvoir greisen fluid to these sites (Monnier et al., 2018, 2020). Disparity in W ore deposition in these veins was a function of the intensity of fracturing, which induced more or less important boiling/flashing of the fluid (Monnier et al., 2020). Although it is recognized that the high temperature greisen fluids were enriched in Sb (Monnier et al., 2018), mineralization did not form in the granite and Sb was transported by the greisen fluid and precipitated in distal veins (Nades) when the fluid cooled (Monnier et al., 2020; 2021b). The third and last stage corresponds to widespread supergene alteration. This consisted in replacement of greisen muscovite and igneous feldspar by kaolinite, partial replacement of wolframite by W-rich goethite, and formation of quartz veins, accompanied by low-temperature minerals such as the phosphate goyazite-gorceixite, fluorite, allophane and Mn-oxydes (Monnier et al., 2019).

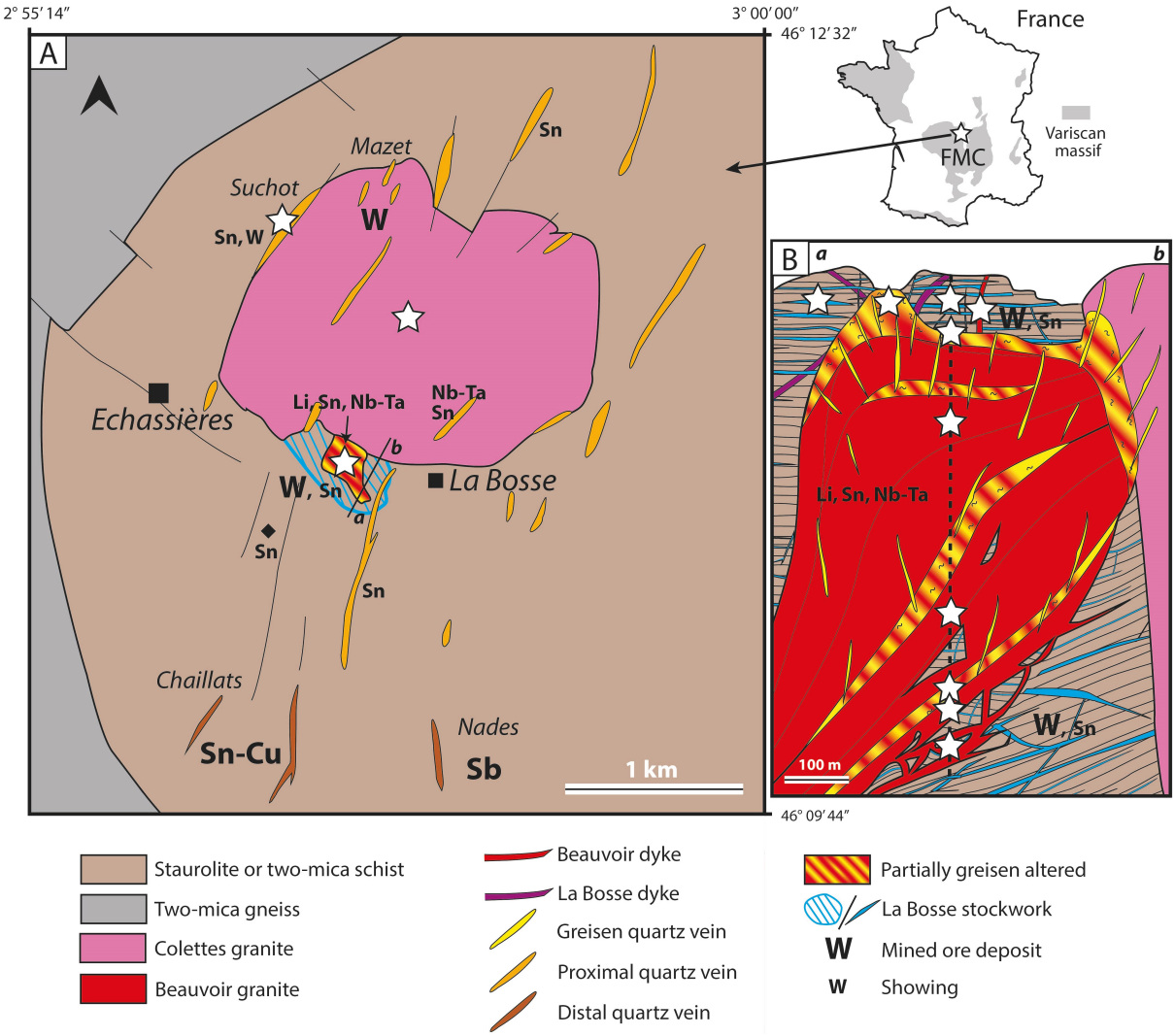

Fig. 1. Simplified geology of the study area. Samples are localized by star symbols. [A]: Geological map of the Echassières district. The a-b segment indicates the cross-section depicted in [B]. [B]: A sketch of the Beauvoir granite along the a-b cross-section, constructed using information from surface outcrops and from a GPF bore-hole projection (deep drilling project of France; located by the dashed line in [B]). Vein and dyke thicknesses are not to scale.

3. Material and methods

Samples consist of outcrop and drill core material that was collected on site or from storage at the French Geological Survey (BRGM, Orleans, France). Thin and thick sections (30 µm and ca. 200 µm, respectively) were prepared from each sample.

The trace-element content of micas was analyzed by LA-ICP-MS using a UV laser-ablation microsampler CETAC® Excite (193 nm) coupled to a ThermoScientific® X serie II quadrupole plasma mass spectrometer, at the BRGM laboratory in Orleans. The laser configuration was optimized by performing multiple trial measurements on several magmatic and hydrothermal micas with different resistance to the laser

impulsion. The laser was equipped with a HelEx® 2 volume ablation chamber. The frequency was 8 Hz, fluency 6 J.cm^{-2}, and spot diameter 50 µm. After ablation, the material is transported by a He flux of 0.3L/min and mixed with an Ar flux if 1L/min, before entering the plasma. The ICP RF power is 1400 W. All micas crystals were analyzed for Li, Na, Mg, Al, K, Ti, Fe, Ge, Rb, Sr, Nb, Sn, Cs, Sb, Ba, Ta, W. Acquisition consisted of 40 s runs (320 laser pulses), separated, before and after, by 20 s of background recording. Presence of mineral inclusions was verified by monitoring the presence of anomalous peaks on the flat part of the signal, and excluded from the integration of the signal. To avoid background noise from analyzes of Rb-rich micas, these micas groups were studied after the Rb-poor micas. Detection limits (d.l.) are given in Table A2 (Appendices) for each element. Acquisition errors are lower than 10 % for concentrations above d.l. by at least 1 order of magnitude. Data reduction was undertaken using Glitter® software, calibrated using NIST SRM 612 as external standard (concentration from Pearce et al., 1997). Silica was used as internal standard reported to values measured by Electron Probe Micro-Analyser (EPMA) for all mica groups considered (Table A1 in Appendices). EPMA were performed at the Centre Castaing - University Paul Sabatier (Toulouse, France) using a CAMECA SXFive. Surface areas of 2x2 µm were analyzed using accelerating voltage 15kV and a beam current of 10nA. The following standards were used for calibration: topaz (F), albite (Na), periclase (Mg), corundum (Al), tugtupite (Cl), sanidine (K), wollastonite (Ca, Si), pyrophanite (Mn), hematite (Fe), Ti (pyrophanite) chromium oxide (Cr), barite (Ba), and Glass Ge-Al-Ca-Rb (Rb).

4. Results

4.1. Petrography

In this section, we describe the main petrographic features of the different magmatic facies and hydrothermal episodes considered in this study, focusing in particular on the characteristics of each mica generation. For specific information on the entire paragenesis and the diverse variety of facies and textures occurring in the area, the reader is referred to Monnier et al. (2018, 2019, 2020), where igneous and hydrothermal textures are fully detailed.

149 *4.1.1. Beauvoir and Colettes granites.*

150 The hololeucocratic equigranular Beauvoir granite is made up of albite, quartz, lepidolite, subordinate
151 variable amounts of topaz and potassic feldspar, plus a wide diversity of accessory minerals (Fig. 2.A').
152 Among these, cassiterite occurs in the entire granite body (Fig. 2.B), while columbo-tantalite and
153 pyrochlore are mostly concentrated in the apex of the granite body. Greisen alteration caused dissolution
154 of the magmatic minerals (Fig. 2.A''), replacing them by various proportions of quartz, muscovite and, to a
155 lesser extent, apatite. In most of the greisen zones, igneous quartz is only partially altered while feldspar
156 and lepidolite were more efficiently removed. In some samples, however, igneous as well as hydrothermal
157 quartz is totally absent and only greisen muscovite replaces magmatic minerals. In this particular case, it is
158 possible to observe relicts of igneous lepidolite, even if all the igneous quartz was dissolved (Fig. 2.C'.C'').
159 Greisen muscovite can be green in color near the edges of quartz veins and at the borders between greisen
160 and fresh rock (Fig. 2.D), while pale-yellow muscovite mainly occurs in the central parts of greisenized
161 areas. The Colettes granite corresponds to a porphyritic two-mica intrusive (Fig. 2.E). The phenocrysts
162 consist of euhedral feldspar and quartz, with subordinate amount of cordierite. Muscovite, brown mica and
163 quartz form the phaneritic matrix (Fig. 2.F).

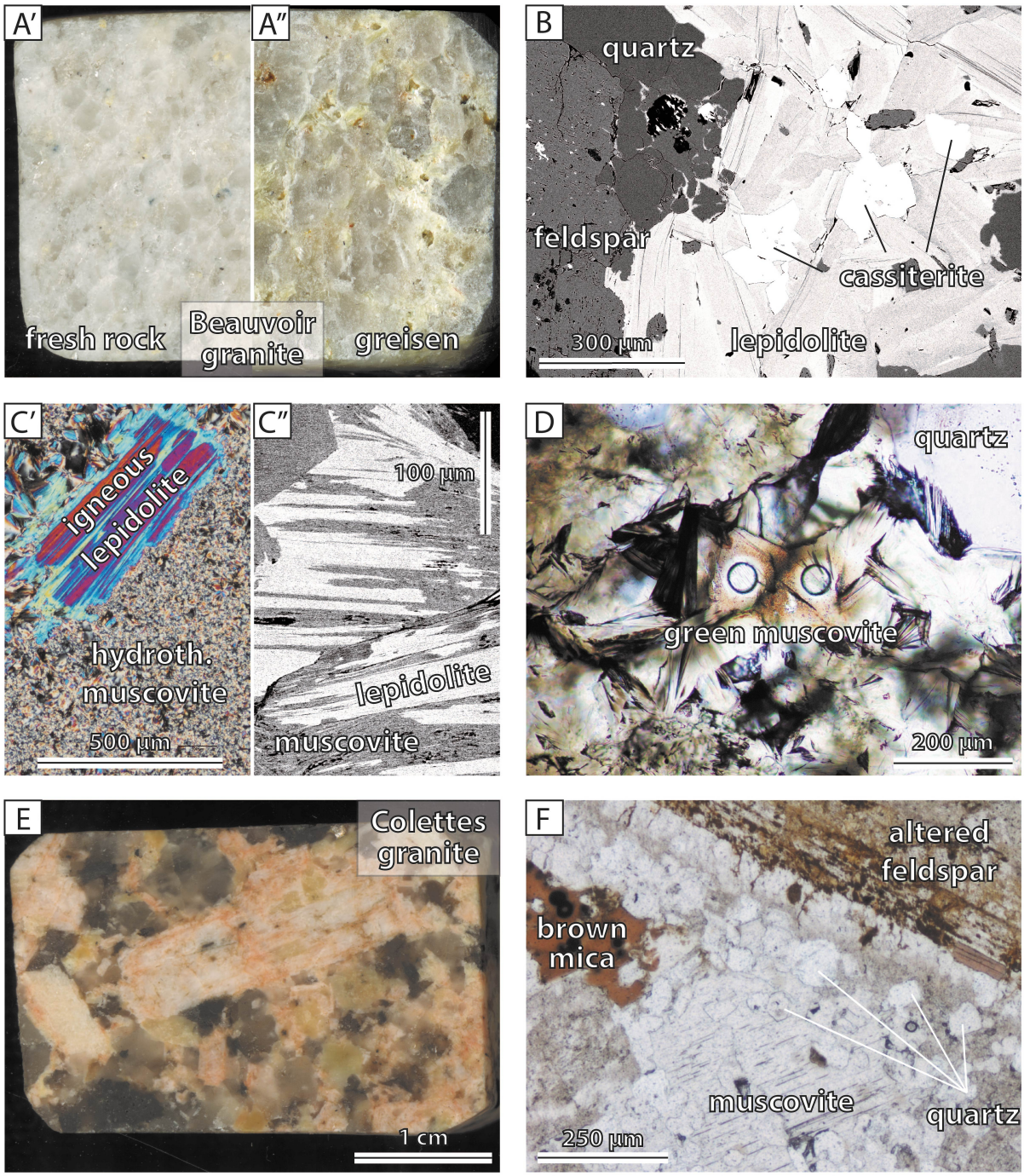

Fig. 2. Petrography of the Beauvoir/Colettes granitic bodies. [A']: high resolution scan of a thin section block showing typical unaltered Beauvoir granite texture. [A"]: High resolution scan of a thin section block depicting quartz-rich greisen. [B]: Scanning Electron Microscopy (SEM) backscattered electron (BSE) image of the typical igneous assemblage of the Beauvoir granite, i.e., feldspar, quartz, lepidolite and cassiterite. [C']: Cross-polarized light (XPL) thin section image of an uncommon greisen texture with lepidolite as the only igneous relict in a sericitized matrix composed exclusively of muscovite (no quartz). [C"]: SEM BSE image illustrating partial replacement of igneous lepidolite by greisen muscovite. In this sample, lepidolite is more strongly altered then other igneous minerals. [D]: Plane-polarized light (PPL) thin section image of greisen samples exhibiting sprays of hydrothermal green muscovite crystals plus quartz. Two laser ablation holes are visible. [E]: High resolution scan of a thin section block from the two-mica Colettes granite. [F]: PPL thin section image of Colettes granite showing textural relationships between zinnwaldite, muscovite and other igneous phases.

4.1.2. The La Bosse stockwork.

A swarm of sub-horizontal quartz veins, known as the La Bosse stockwork (Fig. 1.A,B), is emplaced in the schist and forms the earliest hydrothermal event in the region. These veins exhibit all the later alteration types that have been recorded in the Sioule nappe. The first hydrothermal episode is evidenced by the formation of wolframite (generation *a*) in the quartz veins (Fig. 3.A,C,E), accompanied by formation of alteration haloes in the schist, consisting of brown mica (Fig. 3.F), tourmaline and ilmenite. The second alteration event affected the schist and the quartz veins; it was manifested by formation of topaz veins (Fig. 3.A,B) and consequent pervasive alteration where quartz was replaced by topaz plus a second generation of wolframite (*b*). Other minerals include brown mica, occurring in small amounts within the veins (Fig. 3.D) but abundantly in the alteration halos (Fig. 3.A,B). This alteration was considered as an early F-rich greisen episode of unknow magmatic origin (cf. Monnier et al., 2020). The last magmatic/hydrothermal episode to affect the stockwork was coeval to the crystallization of the Beauvoir granite. Two alteration episodes can be linked to this granite: 1) an F-rich orthomagmatic alteration expressed by crystallization of lepidolite, a second generation of topaz, and columbo-tantalite plus cassiterite, 2) an OH-greisen, marked by the occurrence of muscovite, quartz, apatite, wolframite, minor topaz and cassiterite (Fig 3.B).

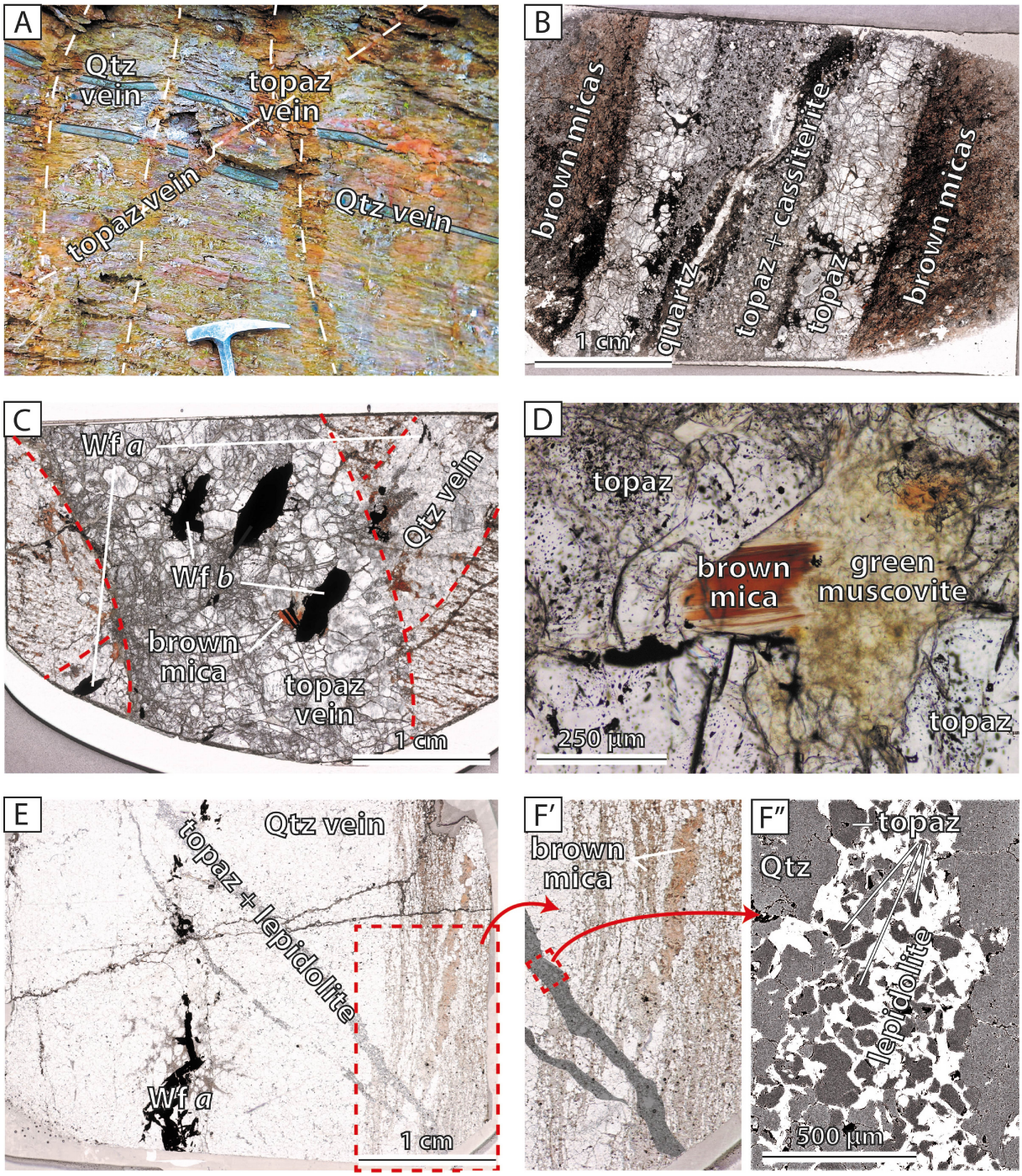

Fig. 3. Petrography of the La Bosse stockwork. Qtz: Quartz; Wf: Wolframite. [A]: Outcrop image showing a detail of The La Bosse stockwork. Quartz veins are transposed along schistosity and intersected by subvertical topaz veins (dashed lines), visible mostly by their alteration halos. [B]: High resolution scan of a thick section depicting a polyphased topaz veins sealed firstly by an early F-rich greisen fluid (topaz) and, at some later time, by a later greisen fluid issued from the Beauvoir granite (topaz and cassiterite). The alteration halo consists mostly of hydrothermal brown micas, accompanied by rutile and monazite. [C]: High resolution scan of a thick section illustrating cross-cutting relationships between an early quartz vein carrying wolframite a and a later topaz vein carrying wolframite b and brown mica. [D]: PPL image of a brown mica crystal partially replaced by green muscovite in the core of a topaz vein. [E]: High resolution scan of a thick section depicting a wolframite a-bearing quartz vein intersected by topaz-lepidolite veinlets. [F']: Zoom on part of image [E] detailing the selvage zone between quartz vein and host schist which is partially obliterated by later metamorphism. The large brown micas crystals containing dark specks of ilmenite and tourmaline differ from the smaller metamorphic biotite in the schist groundmass and are part of the vein's alteration halo. [F'']: SEM BSE image detailing the texture of a topaz-lepidolite veinlet.

4.1.3. The Suchot vein.

A ca. one-meter-thick quartz vein occurs in the Suchot area (Fig. 4.A). Parts of this vein contain minor muscovite (Monnier et al., 2019) and traces of cassiterite (Aubert, 1969). The schist within the vein selvages is strongly affected by alteration halos of several meters in width. Alteration minerals include quartz and two generations of muscovite (a euhedral pale-blue muscovite, Fig. 4.B', replacing anhedral green variety, Fig. 4.B''). Both muscovite generations coexist near the main quartz vein (Fig. 4.C), although blue muscovite fades out as one moves outwards in the selvage. Monazite and rutile crystals are commonly included in the pale-blue (Fig. 4.D') and green muscovite (Fig. 4.D'') varieties, respectively.

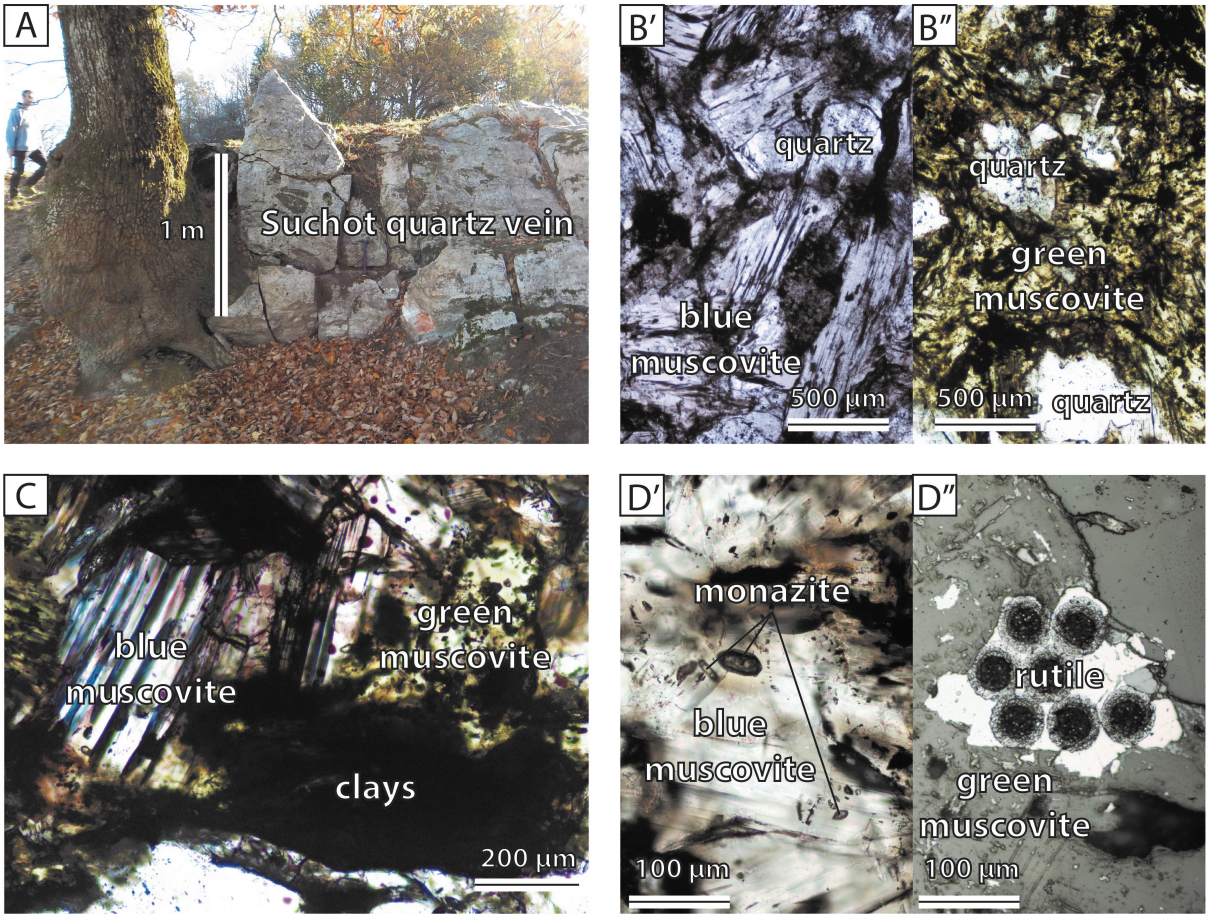

Fig. 4. Petrography of the selvage of the Suchot quartz vein. [A]: Vue of an outcrop showing the meter-scale Suchot vein. [B']: PPL thin-section image of an assemblage of quartz and pale blue muscovite replacing metamorphic minerals in the Suchot vein's selvage. [B'']: PPL thin-section image showing an assemblage of quartz and green muscovite replacing metamorphic minerals in the Suchot vein's selvage. [C]: PPL thin-section image illustrating coexisting pale-blue and green muscovite types. [D']: PPL thin-section image detailing monazite inclusions in pale-blue muscovite. U-Pb dating allowed recognition of two monazite generations, dated at 331±5 and 307±3 Ma (Monnier et al., 2020). [D'']: Reflected light thin-section image of a W-rich rutile grain included in green muscovite. Rutile crystals have been dated at 328±5 Ma (Monnier et al., 2020). Ablation craters are visible.

4.2. Mica characterization

Based on petrographic features, including textural and optical properties as well as occurrences in different assemblages, micas samples were organized into 12 groups. These are listed in Table 1, together with their characteristic features. In the lines below, we classify these groups according to standard parameters based on their major chemical composition. Using the Al-R^{2+}-Si and Li-R^{2+}-Al ternary diagrams and the nomenclature of Monier and Robert (1986) and Foster (1960), a plot of the 12 groups of micas recognized in the Echassières district highlights roughly 3 clusters (Fig. 5). The first cluster, formed by brown mica groups (1), (2) and (3), is located within the biotite-zinnwaldite series, close to the latter end-member. The cluster formed by these 3 groups are hereon referred to as zinnwaldite type. The second cluster, corresponding to micas groups (4), (5) and (6), chemically consists of trilithionite with some polylithionite component, as shown by the Al-R^{2+}-Si ternary diagram (Fig. 5.A). In the rest of the text, we refer to this cluster as the lepidolite type (solid solution between the zinnwaldite, polylithionite and trilithionite poles). Finally, the third cluster is formed by the groups (7), (8), (9), (10), (11) and (12) and is classified as muscovite type, with possibly a minor amount of celadonite component.

Petrographic groups	(1)	(2)	(3)	(4)	(5)	(6)	(7)	(8)	(9)	(10)	(11)	(12)
Micas species	Brown micas (zinnwaldite, see Fig. 5)	Brown micas (zinnwaldite, see Fig. 5)	Brown micas (zinnwaldite, see Fig. 5)	Lepidolite	Lepidolite	Lepidolite	Muscovite	Muscovite	Muscovite	Muscovite	Muscovite	Muscovite
Nature	Hydrothermal	Hydrothermal	Igneous	Hydrothermal	Igneous	Igneous	Hydrothermal	Igneous	Hydrothermal	Hydrothermal	Hydrothermal	Hydrothermal
Picture	Fig. 3.F'	Fig. 3.C,D	Fig. 2.F	Fig. 3.F''	Fig. 2.B,C',C''	Fig. 6.F in Monnier et al., 2019	Fig. 4.B'',C,D''	Fig. 2.F	Fig. 2.C',C''	Fig.3.D	Fig. 4.B,C,D	Fig. 2.D
Sample(s)	001c	P50; 004f	Col-2	001c	P48; P4; BE05; 0003a; BE49; BE54	005f	012a	Col-2	003a	005b; P50	012a	P48
Main petrographic features	Large anhedral crystal in core of quartz veinlets. Abundant ilmenite and tourmaline inclusions	Large subhedral to euhedral crystals. Alteration of schist in vein halo. W-rutile and monazite inclusions	Phenocryst, mm-sized subhedral crystals. Rich in small quartz crystals inclusions	Anhedral small crystal, precipitating around topaz grain.	mm-sized euhedral lath, scarce spray crystals. Common cassiterite inclusions.	mm-sized euhedral lath. Common cassiterite inclusions	Anhedral and disorganized small green crystal, common spray crystal. Abundant W-zoned rutile inclusions	Phenocryst, mm-sized subhedral crystals. Rich in small quartz crystals inclusions.	Disorganized small to large anhedral pale yellow crystal, various cleavage orientation, common spray crystal	Disorganized small green crystal, various cleavage orientation. Alteration of topaz or biotite (2)	Large euhedral to subhedral crystals, pale blue coloured, parallel sheets. Rich in monazite inclusions	Disorganized small to large green, spray, crystals. Alteration of quartz, feldspar and lepidolite (5)
Associated paragenesis (more details in Monnier et al., 2018; Monnier et al., 2019)	Quartz, ilmenite, tourmaline, rutile, native bismuth wolframite a[1]	Topaz I, rutile, wolframite b[1], monazite	K-feldspar, plagioclase, quartz, rutile	Topaz II, cassiterite	Albite, quartz, topaz, cassiterite, columbo-tantalite series, pyrochlore	Albite, quartz, topaz, cassiterite, columbo-tantalite series,	Rutile, monazite,	K-feldspar, plagioclase, quartz, rutile	Apatite, quartz, columbo-tantalite series, pyrochlore	Scarce apatite, Wolframite c[1].	Quartz, monazite, xenotime	Apatite, quartz, columbo-tantalite series, pyrochlore
Location	La Bosse stockwork	La Bosse stockwork	Colettes granite	La Bosse stockwork	Beauvoir granite	La Bosse stockwork	Suchot area	Colettes granites	Beauvoir granite	La Bosse stockwork	Suchot area	Beauvoir granite
Sub location	Quartz vein selvage	Topaz veins; Topaz vein halos	-	Micro veins or pervasive alteration	-	dyke	Suchot quartz vein halo and schist	-	Greisen altered zone	Topaz veins, quartz veins	Suchot quartz vein halo	Greisen altered zone
Age (Monnier et al., 2021a)	>360 Ma	~330-335 Ma	~310 Ma	<360 Ma	~310 Ma	<335 Ma	~330 Ma	~310 Ma	~310[2]	<330 Ma	~310 Ma	~310[2]

Table 1: Main characteristics of micas groups analyzed by LA-ICP-MS. [1] Three types of wolframite (a, b and c) occurs in the Echassières district, see Monnier et al., 2019 and Monnier et al., 2020, for further information about W ore. [2] Beauvoir greisen muscovite or associated minerals has not been directly dated, nevertheless greisen alteration initiated at hot temperature (Monnier et al., 2020), during cooling of the Beauvoir granite which crystallized at ca. 310 Ma (Monnier et al., 2021a and references within).

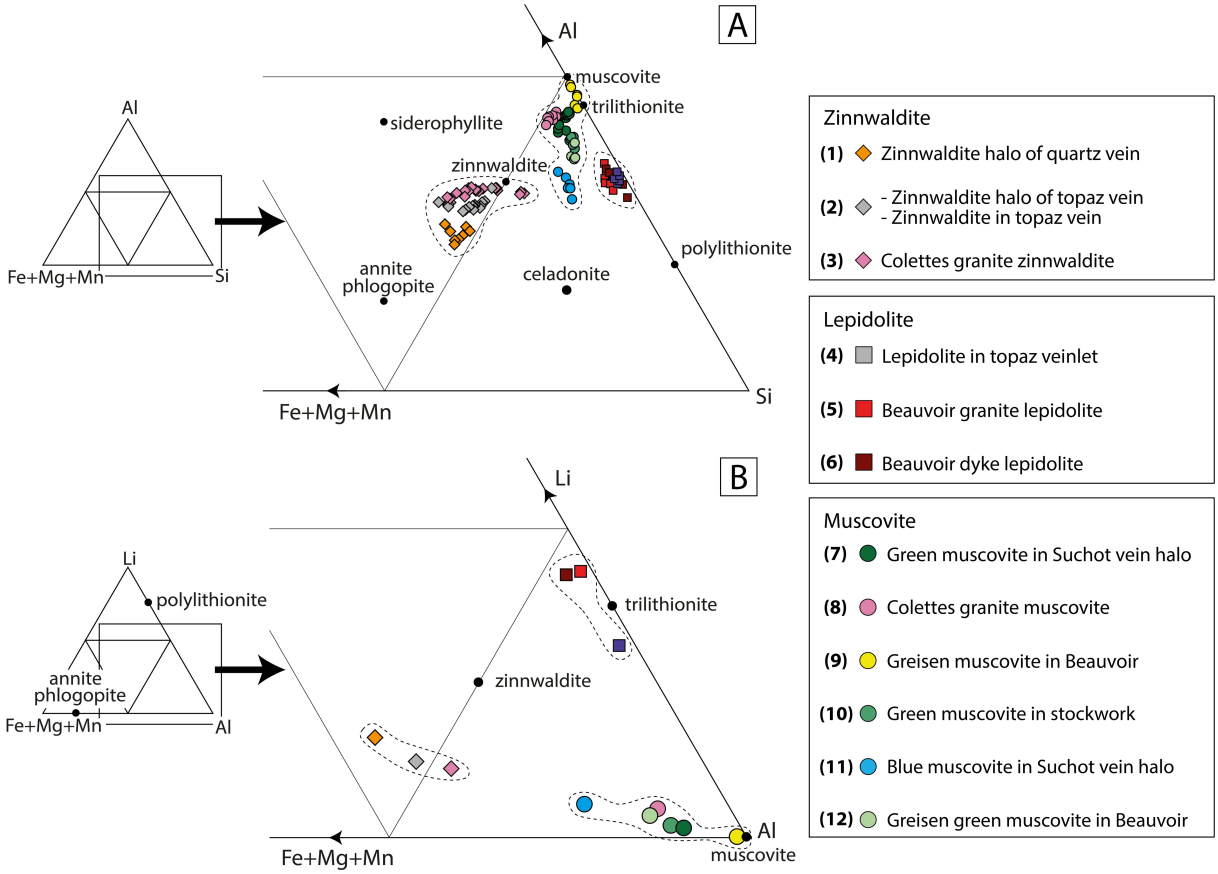

Fig. 5. Mica classification ternary diagrams (Foster, 1960; Monier and Robert, 1986). Diagram [A] is constructed using EPMA data while diagram [B] is constructed using mean Li values obtained by LA-ICP-MS (undetectable with the EPMA protocol), together with EPMA data. Each group is identified by a number (in brackets) and a colored symbol, consistent through the following text and Figures. Diamonds, squares and circles correspond respectively to symbols for brown micas, lepidolite and muscovite series.

The three types of micas defined above (zinnwaldite, lepidolite, muscovite) are also well distinguished by their respective Li contents (Fig. 6). Lepidolite exhibits the highest Li concentrations (ca. 10,000 to 30,000), zinnwaldite has intermediate contents (ca. 4000 to 10,000 ppm), while muscovite is relatively Li-poor (few ppm to ca. 3000 ppm).

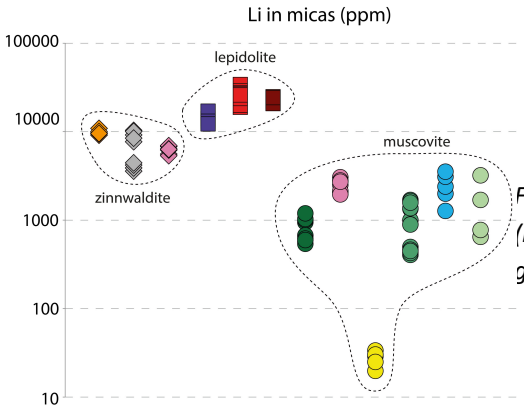

Fig. 6. Univariate diagram depicting the range of Li concentrations (measured by LA-ICP-MS) for the different mica petrographic groups. Symbols as in Fig. 5.

Regarding other elements, below are described only the most remarkable results, and the reader is referred to Table 2 for average concentrations of trace elements for each petrographic group, and to Table A2 (Appendices) for the full dataset. Tin is relatively enriched (tens to ca one thousand ppm) in all mica groups compared to other micas from W-Sn deposits (Codeço et al., 2021), and is strongly enriched in muscovite (9) and (12) from the Beauvoir greisen (ca. 1000 and 1400 ppm in average for yellow and green muscovite, respectively; Fig. 7.A). Such concentrations (more than 1000 ppm) have only been recorded in muscovite from the Cinovec granite during late greisen alteration, called “muscovitization” by Breiter et al. (2019). The Ta/Nb ratio is highest (> 4) for the (9) and (12) muscovite groups from the Beauvoir greisen and lowest (< 0.1) for zinnwaldite from the topaz veins (2). Ta and Nb are globally enriched (> to 20 ppm and 100 ppm, respectively) in igneous micas (Fig. 7.B). Rubidium is strongly enriched in lepidolite and zinnwaldite from quartz vein halos (1), with concentrations mostly superior to 10 000 ppm (Fig. 7.C). Cesium content is also particularly high (ca. 7000 ppm in average) in these micas (1), and low in the muscovite groups and in zinnwaldite from topaz veins (< 600 ppm; Fig. 7.C). Tungsten is remarkably enriched, with more than 100 ppm in average in lepidolite (4), (5), (6), in muscovite from the Colettes granite (8) and in green muscovite (7) from the Suchot area (Fig. 7.D). In some samples of lepidolite from the Beauvoir granite (5), W concentrations can reach 300 ppm, which, to our knowledge, is the highest W content in mica ever reported in the literature. Titanium contents are low in lepidolite and muscovite groups, except for muscovite in the Colettes granite (8) and green muscovite of the Suchot area (7), which display concentrations of ca. 4000 ppm, while zinnwaldite are the most Ti-enriched mica species, with ca. 10,000 ppm in all the three groups (Fig. 7.D). We noticed that all magmatic or hydrothermal micas with Ti concentrations higher than ca. 1000 ppm are associated with a Ti-phase, either rutile or ilmenite. Conversely, micas with subordinate Ti contents are not coeval with Ti-bearing minerals. Barium is enriched in hydrothermal micas (from ca. 50 to 900 ppm in average) and depleted in magmatic micas (<20 ppm in average; Fig. 7.E). Magmatic micas are also strongly depleted in Sr (<0.3 ppm in average), which can exceed 10 ppm in zinnwaldite from topaz veins (2) and in green muscovite from the Suchot area (7). Germanium varies only slightly, averaging 6 ppm in zinnwaldite from the Colettes granite (3), and 1.5 ppm in greisen

muscovite from the Beauvoir granite (9), (12). A noteworthy observation is that, with few exceptions, in the Echassières district, W-rich micas are relatively depleted in Sn, and vice versa (Fig. 7.F).

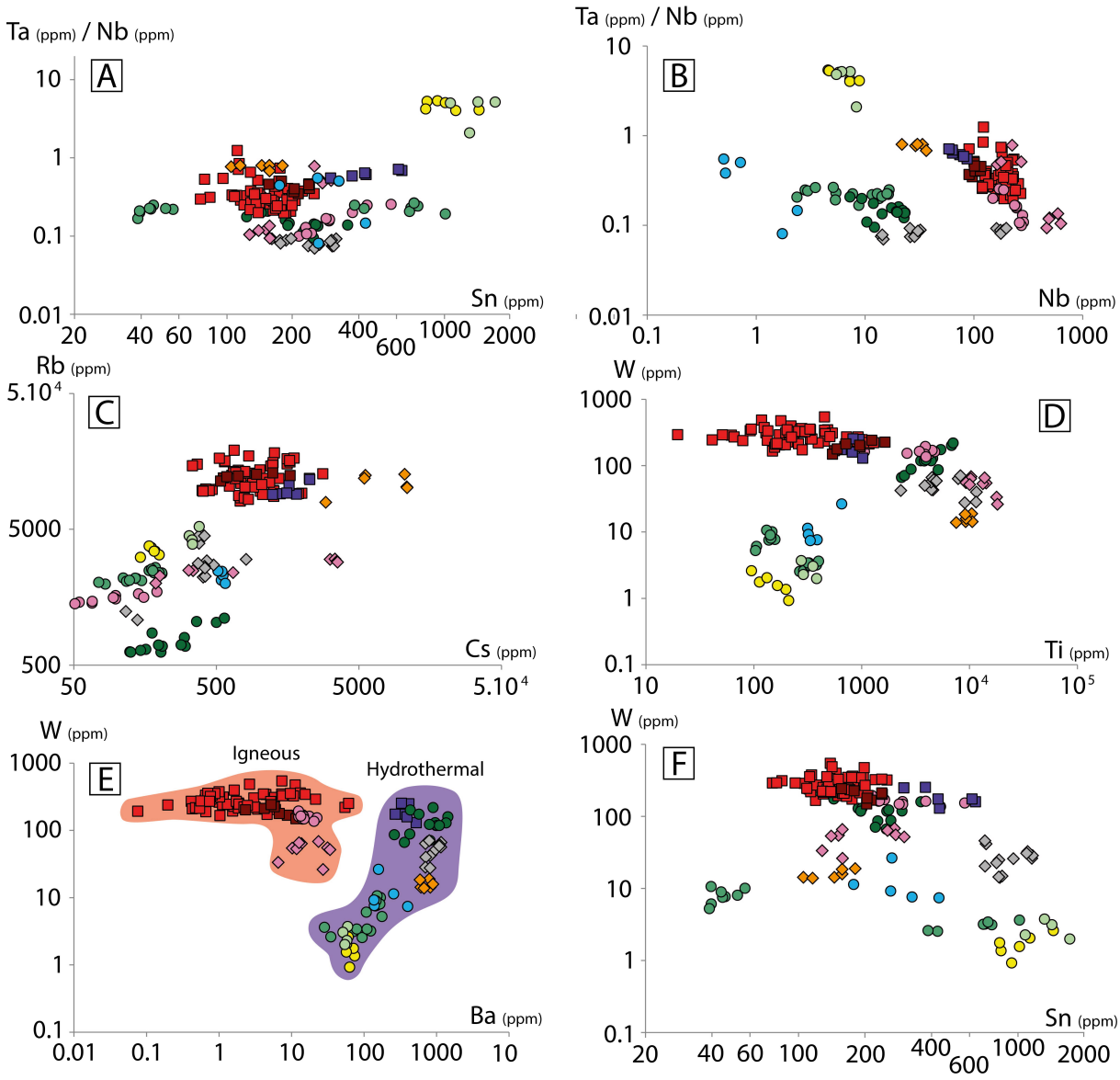

Fig. 7. Binary diagrams depicting LA-ICP-MS data for selected element pairs, for the different petrographic groups. The red and violet shapes in E correspond respectively to igneous and hydrothermal mica groups. Symbols as in Fig. 5.

A remarkable feature emerging from these results is that groups that contain micas originating from different samples, such as (2), (5) and (10) have homogeneous signatures (cf. Table 1), with the exception of a few elements such as Sn for group (10) and Nb for group (2) that vary strongly across samples. Another notable feature is the homogeneous signature of group (2) mica, given that this group contains zinnwaldite from both core and alteration halos of topaz veins, located above and below the Beauvoir granite. Signatures are also homogeneous within single-sample groups, excepted few elements which display significant variations, such as Cs and Sn in zinnwaldite from the Colettes granite (3).

group	(1) n=6		(2) n=13		(3) n=9		(4) n=6		(5) n=58		(6) n=7	
ppm	mean	S.D.	mean	S.D.	mean	S.D.	mean	S.D.	mean	S.D.	mean	S.D.
Li	9763	564	7209	2590	6204	616	14782	1873	24619	3420	23104	1320
Na	1223	171	2201	760	2395	134	1458	154	2647	415	2191	246
Ti	9391	1022	6305	2895	13958	0.34	827	129	351	305	174	23
Ge	4.13	0.79	4.05	1.16	6.13	1.91	3.21	1.21	3.44	1.16	3.39	0.74
Rb	10884	1672	2798	1000	2516	359	9756	974	12333	2810	12263	503
Sr	1.6	0.5	13.1	2.5	0.1	0.0	Bdl	-	Bdl	-	Bdl	-
Nb	30.9	4.7	26.2	9.4	419.1	169.6	71.3	10.0	177.3	40.1	103.3	8.6
Sn	143	26	246	57	193	64	467	122	152	37	205	28
Cs	7704	3174	397	158	1427	1500	1653	326	986	489	893	388
Ba	732	113	899	166	18	9	376	82	5	10	6	2
Ta	23.8	3.2	2.2	0.9	81.8	38.8	44.5	2.6	63.2	26.8	42.9	6.7
W	15.9	2.0	49.9	13.4	48.2	15	189.4	45.5	286.3	75.8	183.5	37.12

group	(7) n=14		(8) n=10		(9) n=6		(10) n=16		(11) n=5		(12) n=4	
ppm	mean	S.D.	mean	S.D.	mean	S.D.	mean	S.D.	mean	S.D.	mean	S.D.
Li	734	203	2407	277	27	4	871	481	2451	795	1578	1021
Na	6385	484	6211	833	564	137	364	107	637	54	325	70
Ti	4364	1364	3582	1010	153	43	233	104	402	128	325	45
Ge	3.68	0.35	3.99	1.14	1.49	0.48	1.97	0.73	4.27	0.49	2.38	0.52
Rb	771	166	1548	102	3445	228	2277	193	2263	185	4435	500
Sr	18.8	6.8	0.2	0.1	0.3	0.1	0.4	0.3	6.7	4.8	0.2	0.1
Nb	16.7	5.4	234.0	45.5	6.4	1.5	9.1	5.1	1.2	0.8	6.8	1.1
Sn	223	61	319	107	1031	214	362	343	293	85	1385	233
Cs	261	132	102.0	44	176	16	152	41	548	21	344	21
Ba	817	352	15	3	64	6	113	46	219	101	54	3
Ta	2.4	0.7	36.1	6.4	29.1	3.9	2.0	1.2	0.3	0.1	28.3	7.6
W	128.3	44.1	159.2	14.8	1.7	0.5	5.6	2.7	12.4	7.1	2.8	0.7

291 *Table 2: Mean and standard deviation of element concentrations for the petrographic mica groups, analyzed by LA-ICP-MS.*

4.3. Chemical signatures and identification of mica generations

In order to properly examine the large trace-element dataset for all mica groups, we implemented a panel of multivariate statistical analyses, namely, Principal Component Analysis (PCA) ordination, Hierarchical Cluster Analysis (HCA), and Permutational Analysis of Variance (PERMANOVA). All these multivariate analyses were monitored with the software Past 3.17 (Hammer et al., 2001). The few data that fell below the limits of detection (available in table A2, Appendices) were considered as equal to the given limit (almost exclusively Sr measurement for igneous micas). Statistical distance of similarity were calculated with the Bray Curtis similarity index (Bray and Curtis, 1957). A similarity distance equal to 1 means that the two analyses considered are strictly equal for all elements measured, and as the distance decreases, the difference increases. This protocol was also used to characterized trace-element signatures in quartz from the Echassières and other Sb districts in France (Monnier et al., 2018, 2021b). HCA and PCA are statistical tools that are becoming of common use in the geochemical literature (cf., Lin et al., 2014 and Codeço et al., 2021, for other applications in the field of economic geology). Anderson (2001) provides a detailed description of the PERMANOVA test. See Supplementary Material for a brief explanation of process and objectives for each specific multivariate analysis.

4.3.1. Principal Component Analysis.

The first PCA ordination (Fig. 8) was calculated using all elements analyzed (i.e., major and trace elements). As expected, the first and the second components (which best represent the entire data) discriminate well the different types of mica (lepidolite, zinnwaldite and muscovite groups), notably by their enrichment in Na, Al and K for the muscovite groups and in Fe and Mg for the zinnwaldite groups (Fig. 8.A). Only the third component seems to group different mica species, in particular muscovite (3) and zinnwaldite (8) from the Colettes granite on one hand, and the majority of hydrothermal micas on the other (Fig. 8.B). To obviate artifacts owing to a specific mineral's nature, we repeated the PCA excluding major elements (K, Al, Na, Fe, Mg) and Li, which are variably enriched depending on the type of mica (Fig. 6). The second PCA ordination (Fig. 9) forms several clusters that are characterized by the same positive and negative correlations. Ba and Sr are particularly enriched in zinnwaldite of topaz veins (2) and in green muscovite in Suchot vein halos (7);

they are depleted in igneous micas (3), (5), (6), (8) and hydrothermal lepidolite from the La Bosse stockwork (4) for the principal component. Niobium, Ta, W and Rb enrichment characterizes the group of igneous micas. Germanium is enriched in Colettes Zinnwaldite (3), and Sn is particularly enriched in greisen muscovite of the Beauvoir granite. The remaining muscovite groups (10) and (11) are not so much characterized by an Sn enrichment as by the Ba-Sr couple. On a first order, Ti is more enriched in zinnwaldite (1); (2); (3), in agreement with numerous studies which report the presence of up to 7 w.% of TiO_2 in biotite from various origin (e.g., Thompson et al., 1997; Cesare et al., 2008; Wu and Chen, 2015. Nevertheless, some muscovite, (7) and (8), displays Ti concentrations (ca. 4000 ppm) only slightly inferior then those in zinnwaldite (2), roughly equals to 6000 ppm.

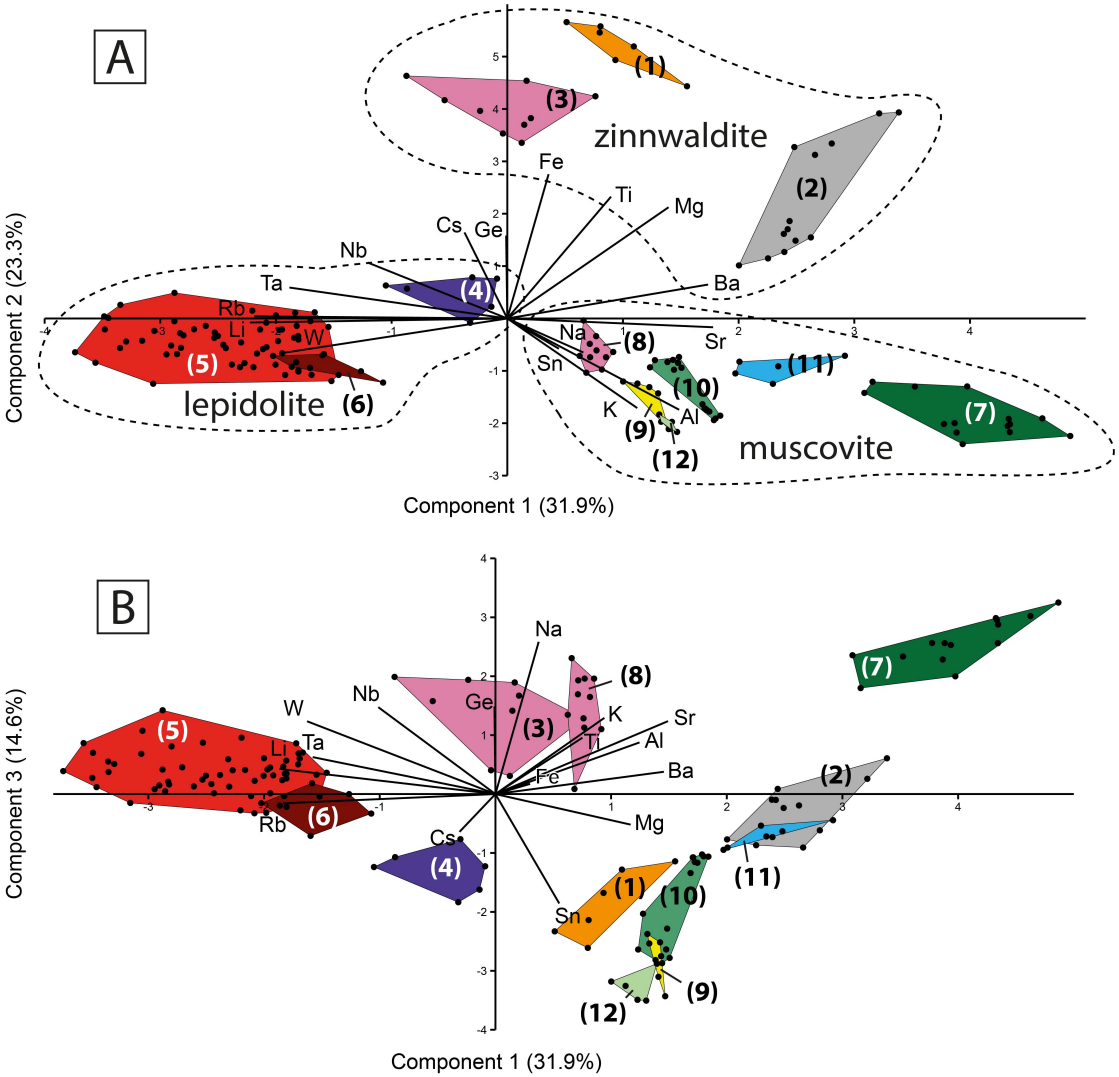

Fig. 8. Principal component analysis (PCA) diagrams projecting components 1 and 2 [A] and 1 and 3 [B] for all trace and major elements analyzed by LA-ICP-MS. The different mica species are identified and clustered in [A] by the dashed lines. Shape colors and numbers refer to mica groups (cf. Fig. 5).

In brief, PCA ordination of trace elements discriminates three distinct clusters, mainly by the first component: i) igneous micas and hydrothermal lepidolite (3), (4), (5), (6) (8), ii) zinnwaldite in quartz vein halos (1), iii) and a last cluster including the other hydrothermal micas (2), (7), (9), (10), (11), (12). We can subdivide the first and the third clusters using the second and third component: micas from the Colettes granite (3) and (8) are distinguished from the lepidolite groups (4), (5), (6), and the (2) and (7) mica groups are distinguished from muscovite (9), (10), (11), (12), particularly for greisen muscovite in the Beauvoir granite. Remarkable elemental associations include the Ba-Sr and W-Rb couples, which are strongly correlated in micas from the Echassières district. Conversely, Cs and Rb are only slightly correlated, although these elements occupy the same site in the lepidolite micas series.

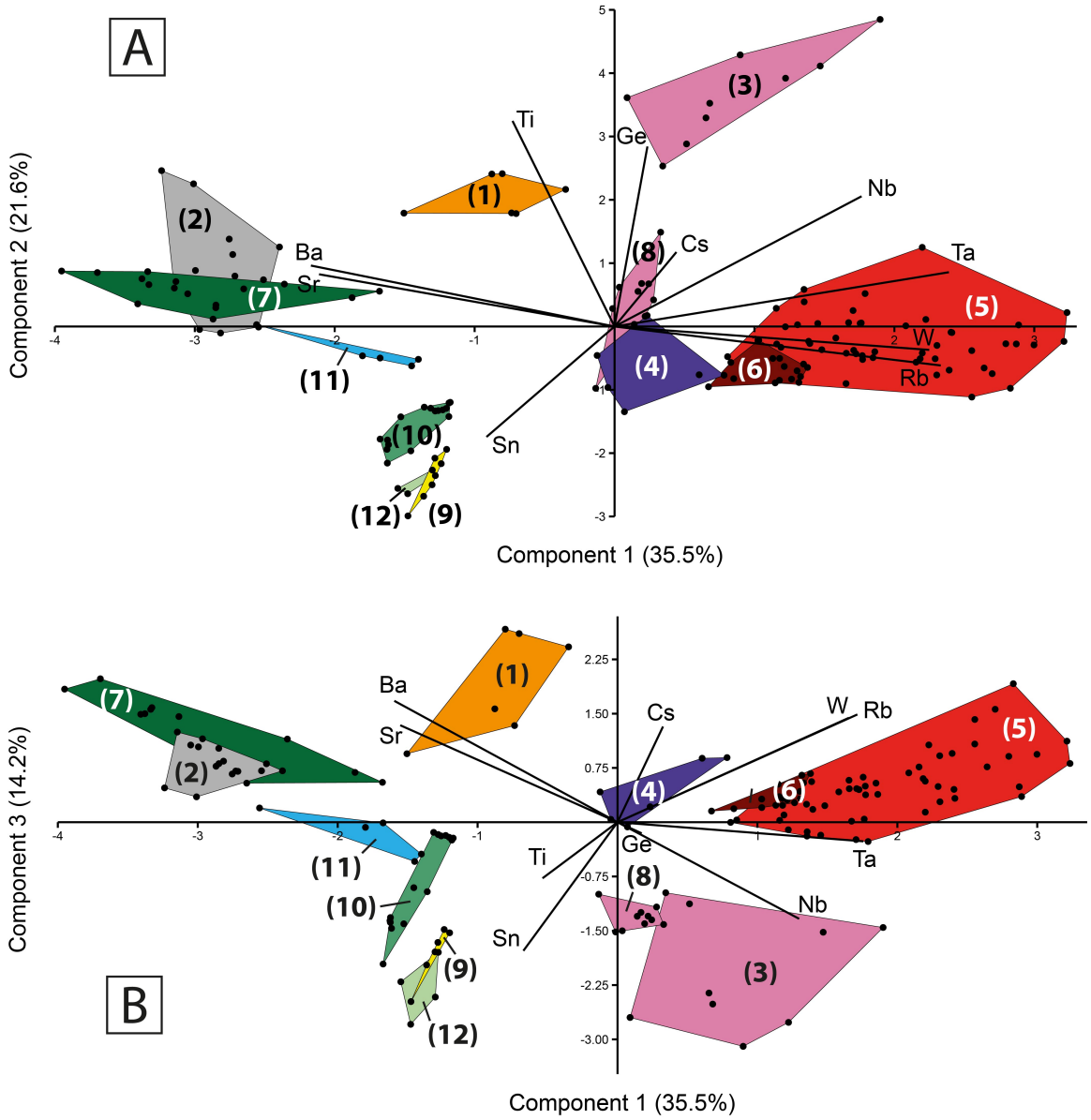

Fig. 9. PCA diagrams projecting components 1 and 2 [A] and 1 and 3 [B] for selected trace elements (Ti, Ge, Rb, Sr, Nb, Sn, Cs, Ba, Ta, W) analyzed by LA-ICP-MS. Shape colors and numbers refer to mica groups (cf. Fig. 5).

4.3.2. Hierarchical Cluster Analysis.

At a first glance, HCA for all groups (Fig. 10.A) confirms that each petrographic mica group (with the exception of the (6), (5) and (12), (9) couples, discussed below) displays a unique and homogeneous trace-element signature, as each analysis assembles mostly the same clusters that already belonged to the different petrographic groups. Similarly, micas groups that include several samples, i.e. (2), (5), (10) are characterized by unique, coherent signatures, as previously noted. This is not entirely the case for the two samples of stockwork green muscovite (10), which are clearly separated but occupy nearby clusters in the dendrogram, suggesting limited differences in their chemical signatures. Some petrographic groups, (5) and (6) on one hand and (9) and (12) on the other, display very similar chemistry and form undiscernible

clusters. These results imply that chemical signatures of lepidolite from dykes (6) and from the main body of the Beauvoir granite (5) are almost undistinguishable, as for green (12) and pale-yellow muscovite (9) in the Beauvoir granite, in accordance with obvious genetic links which connect these two groups. We can highlight the resemblance of some mica groups by clustering; for example, groups (2) and (7) form a cluster with a similarity of ca. 0.7, and mica groups from the Colettes granite (3) and (8) have a similarity of ca. 0.6. Hydrothermal lepidolite (4) displays a similarity of ca. 0.7 with the igneous micas from Beauvoir granite (5) and (6), in the same way that one sample of greisen muscovite from stockwork (10) and the Beauvoir greisen muscovites (12) and (9). The second sample of muscovite (10) is clearly more distant, sharing a similarity of less than 0.5 with the latter cluster. Two other mica groups that display relatively low similarity values with other groups are zinnwaldite in quartz vein halos (1) and greisen blue muscovite at Suchot (11). Zinnwaldite in quartz vein halos (1) is not closely associated with other groups. The group of blue muscovite (11) is close to the cluster (2) and (7), as it has been previously highlighted by similar elemental correlation, notably Ba and Sr, in PCA (Fig. 9). However, when we consider only the hydrothermal micas group (Fig. 10.B) in a novel HCA, we observe a major difference which consists of the location of the blue muscovite groups, closely associated (similarity of ca. 0.6) to one sample of greisen muscovite from stockwork (10). This outcome implies that blue muscovite (11) and Beauvoir greisen muscovite (12) and (9) are relatively analogous to green muscovite from the stockwork (10), while mica groups (11) on one hand and (12) and (9) on the other, are more different from each other. In other terms, green muscovite from the stockwork (10) seems to have intermediate composition between two chemical poles consisting of blue muscovite (11) and by Beauvoir greisen muscovite groups (12) and (9). Also, due to the absence of igneous lepidolite in the Beauvoir granite (6), (5), hydrothermal lepidolite disposition differs from the first HCA and forms, with zinnwaldite in quartz vein halos (1), a cluster of similarity ca. equal to 0.6.

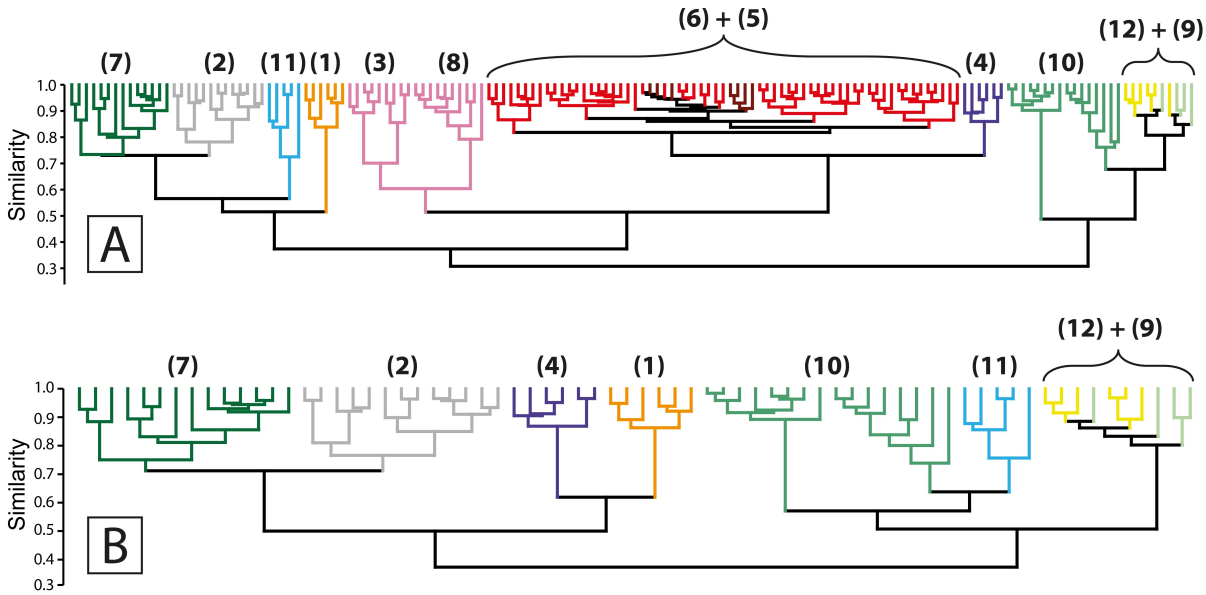

Fig. 10. [A]: Dendrogram resulting from hierarchical cluster analysis (HCA) of the same panel of trace element data as in Fig. 10 (i.e., Ti, Ge, Rb, Sr, Nb, Sn, Cs, Ba, Ta, W), considering all the petrographic mica groups. [B]: Dendrogram resulting from HCA of the above elements, excluding the (3), (5), (6) and (8) petrographic groups (igneous micas). Shape colors and numbers refer to mica groups (cf. Fig. 5).

In summary, the most significant results of HCA are similar to those obtained by PCA, i.e, highlighting a strong affinity between mica groups (7) and (2), as well as for hydrothermal lepidolite (4) and igneous lepidolite from the Beauvoir granite (5) and (6), and a clear similarity between zinnwaldite and muscovite from the Colettes granite. Muscovite (9), (10), (11) and (12) also display similar chemistry, whereby the greatest difference was found between blue muscovite from Suchot veins (11) and greisen muscovite from the Beauvoir granite (9) and (12). Finally, zinnwaldite in quartz vein halos (1) shares limited similarities with the hydrothermal lepidolite (4).

4.3.3. Permutational Analysis of Variance.

group	(1)	(2)	(3)	(4)	(5)	(6)	(7)	(8)	(9)	(10)	(11)	(12)
(1)		0.01	0.03	0.16	0.01	0.02	0.01	0.02	0.09	0.01	0.13	0.4
(2)	0.01		0.01	0.01	0.01	0.01	0.01	0.01	0.01	0.01	0.01	0.03
(3)	0.03	0.01		0.02	0.01	0.01	0.01	0.01	0.01	0.01	0.03	0.13
(4)	0.16	0.01	0.02		0.03	0.05	0.01	0.03	0.15	0.01	0.1	0.33
(5)	0.01	0.01	0.01	0.03		1	0.01	0.01	0.01	0.01	0.01	0.01
(6)	0.02	0.01	0.01	0.05	1		0.01	0.01	0.04	0.01	0.06	0.25
(7)	0.01	0.01	0.01	0.01	0.01	0.01		0.01	0.01	0.01	0.01	0.02
(8)	0.02	0.01	0.01	0.03	0.01	0.01	0.01		0.02	0.01	0.03	0.07
(9)	0.09	0.01	0.01	0.15	0.01	0.04	0.01	0.02		0.01	0.09	0.32
(10)	0.01	0.01	0.01	0.01	0.01	0.01	0.01	0.01	0.01		0.55	0.01
(11)	0.13	0.01	0.03	0.1	0.01	0.06	0.01	0.03	0.09	0.55		0.48
(12)	0.4	0.03	0.13	0.33	0.01	0.25	0.02	0.07	0.32	0.01	0.48	

385

≤0.05 >0.05

386 *Table 3: Permanova p-values between all groups considering the same panel of trace element data as in Fig. 9*
387 *and Fig. 10 (i.e., Ti, Ge, Rb, Sr, Nb, Sn, Cs, Ba, Ta, W). The f-values are available in Table 4.*

gr.	(1)	(2)	(3)	(4)	(5)	(6)	(7)	(8)	(9)	(10)	(11)	(12)
(1)		30.74	29.13	61.23	72.71	98.42	84.52	119.1	232.9	217.8	185.8	126.3
(2)	30.74		18.09	52.75	260.8	87.66	13.07	19	48.25	95.63	32.39	30.59
(3)	29.13	18.09		110.7	271	167.3	64.65	62.27	120.9	178.9	90.54	77.6
(4)	61.23	52.75	110.7		9.17	36.57	125.4	150	246	152.6	201	109.7
(5)	72.71	260.8	271	9.17		1.09	473.3	313.9	132.5	391.1	131.7	63.37
(6)	98.42	87.66	167.3	36.57	1.09		203.4	240.4	530.3	220	432.7	261.6
(7)	84.52	13.07	64.65	125.4	473.3	203.4		17.66	133.4	196.3	74.83	86.96
(8)	119.1	19	62.27	150	313.9	240.4	17.66		118.4	118	69.53	84.41
(9)	232.9	48.25	120.9	246	132.5	530.3	133.4	118.4		21.86	70.71	14.23
(10)	217.8	95.63	178.9	152.6	391.1	220	196.3	118	21.86		10.11	32.86
(11)	185.8	32.39	90.54	201	131.7	432.7	74.83	69.53	70.71	10.11		61.21
(12)	126.3	30.59	77.6	109.7	63.37	261.6	86.96	84.41	14.23	32.86	61.21	

388

≤ 2 ≤ 2; > 15 ≤ 15; > 50 ≤ 50; > 100 ≤ 100

389 *Table 4: Permanova f-values between all groups considering the same trace elements as in Fig. 9 and Fig. 10*
390 *(i.e., Ti, Ge, Rb, Sr, Nb, Sn, Cs, Ba, Ta, W). The p-values are available in Table 3.*

391 We are not going to comment on single Permanova results (Tables 3, 4), but we will highlight remarkable
392 results with respect to the previous multivariate analyses. Note that groups with the smallest population,
393 e.g. (1), (4), (9), (11), (12) are subject to higher p-value data, due to possible high variations in
394 concentration coupled to possible low replicates. F-values are less affected by such bias. Zinnwaldite in
395 quartz vein halos (1) exhibits marked differences from most of the other groups, even if their chemistry is
396 closer to that of the other zinnwaldite groups (f-value ≈ 30). Zinnwaldite (2) is also well distinguished by p-
397 value from the other groups, although the difference is less substantial (f-value = 13) for the green
398 muscovite (7). Much as the previous zinnwaldite groups, the Colettes zinnwaldite (3) differs clearly from
399 the other mica groups. The least difference is with zinnwaldite (2), as revealed by the smallest f-value
400 between the two groups. This contrasts with the PCA and HCA results, which had suggested a stronger
401 similarity of Colettes zinnwaldite (3) with the Colettes muscovite (8). The chemistry of hydrothermal
402 lepidolite (4) is close to that of igneous lepidolite (5) and (6). Igneous lepidolite from the Beauvoir main
403 body (5) and dyke (6) displays an indistinguishable trace element signature (p-value = 1; f-value = 1). Green
404 muscovite from the Suchot area shares the lowest f-value with zinnwaldite from topaz veins (2). Colettes
405 muscovite (8) chemistry is close to that of the green muscovite from the Suchot area (7) as well as to that of
406 zinnwaldite from topaz vein (2). As for the Colettes zinnwaldite, results of PERMANOVA on Colettes

muscovite disagree with the previous multivariate analyses. Micas originating from Beauvoir greisen, i.e.,(9) and (12), display a similar chemistry, (p-value = 0.32 ; f-value = 14) and are both relatively close (f-value of 22 and 33) to green muscovite from La Bosse stockwork (10). Finally, blue muscovite from quartz halos in Suchot veins (11) exhibits a strong chemical affinity (p-value = 0.55; f-value = 10) with the green muscovite from La Bosse stockwork (10).

To resume, PERMANOVA confirms most of the relationship highlighted by the previous statistical analyses, i.e., i) an affinity between igneous lepidolite from Beauvoir (5) and (6), and hydrothermal lepidolite (4) from the La Bosse stockwork, ii) an affinity between zinnwaldite from topaz veins (2) and green muscovite from Suchot area (7), iii) a similarity between muscovite (9), (10), (11) and (12), iv) as well as the singular signature of zinnwaldite (1). Nonetheless, the similarity between micas from Colettes granite suggested by the PCA and HCA is not verified by PERMANOVA. We can potentially attribute the large f-value of ca. 62 for Colettes' zinnwaldite and muscovite as the result of chemical differences induced by different partition coefficients between the muscovite and Fe-Mg rich species (Stepanov et al., 2014). Indeed, PERMANOVA is more affected by absolute concentration variations while PCA relationships are best constrained by the correlation, positive or negative, of trace-element for the different groups, which remains essentially the same for muscovite and zinnwaldite from Colettes.

4.3.4. Key results of multivariate analyses.

Considering all results from the different multivariate analyses, we obtain several group connections based on trace-element similarities: i) igneous mica from the Colettes granite (3) and (8); ii) igneous and hydrothermal lepidolite (4), (5) and (6); iii) zinnwaldite from quartz vein halos (1) that are well distinguished from the other groups; iv) green muscovite from the Suchot area (7) and zinnwaldite from topaz veins (2); v) all remaining muscovite groups (9), (10), (11), (12). Nevertheless, the link between the chemical signatures of the blue muscovite from the Suchot vein (11) and greisen muscovite from the Beauvoir granite (9) and (12) would have been hard to pinpoint without the group of green muscovite from the stockwork (10), which exhibits intermediate chemistry.

5. Discussion

5.1. Micas signatures

5.1.1. Matching geochronological constrains to W-Sn mineralizations.

In the Echassières district, the La Bosse stockwork event preceded the Barrovian metamorphism dated at 350-360 Ma (Do Couto et al., 2016, Monnier et al., 2021a). Zinnwaldite (1) from quartz vein halos, considering that quartz vein emplacement and selvage alteration were coeval, may originate from the older hydrothermal event recognized in the Echassières district. This is consistent with the particular signature of zinnwaldite (1), which contrasts clearly with that of the other micas. The topazification episode affected the La Bosse stockwork at ca. 330-335 Ma (Monnier et al., 2021a). Strong textural evidence links zinnwaldite (2) to this F-rich alteration. Moreover, minerals dated at ca. 330 Ma in the Suchot vein area occur as inclusions in the green muscovite group (7), which displays chemical similarities with the zinnwaldite (2). Based on these chemical and chronological evidences, we interpret zinnwaldite (2) and muscovite (7) to originate from the same mineralizing fluid that was responsible for the topazification of the La Bosse stockwork. Despite green muscovite (7) being located in the alteration halo of the Suchot vein, our data and previous ages (Monnier et al., 2021a) show that this mica group should be considered as an inherited generation with respect to the formation of the Suchot vein, i.e., it was present before vein formation. Consequently, the topazification that we observed at the La Bosse stockwork seems to have had a regional influence (or at least was part of a more widespread episode). The Colettes and Beauvoir granites crystallized contemporaneously, at ca. 310 Ma. Expectedly, muscovite and zinnwaldite from the Colettes granite share a roughly homogeneous chemical signature. Yet, lepidolite from the different facies of the Beauvoir granite (5) and (6), exhibits a very consistent signature that differs clearly from that of Colettes' micas. Remarkably, hydrothermal lepidolite (4) associated with the second generation of topaz in the stockwork, and igneous lepidolite (5) and (6), show analogous signatures, implying a roughly similar chemistry for the Beauvoir granitic melt and exsolved fluid during late crystallization stage. The late Sn-W mineralizing episode consists of OH-rich greisen alteration occurring during cooling of the Beauvoir granite (ca. 310 Ma). Hydrothermal muscovite in the different greisen facies of the Beauvoir granite (12) and (9) are chemically related to green muscovite (10) that replaced minerals in the topaz vein, which formed at ca. 330 Ma. Blue muscovite of the

greisen-related Suchot vein halo (11), which exhibits monazite inclusions dated at 307 ± 3 Ma, shows chemical similarities with green muscovite (10) of the stockwork. Based on the strong trace-element affinity with other greisen muscovite (constrained at ca. 310 Ma), and on the relative timing of green muscovite (10) in the stockwork (postdates the 330 Ma topazification episode, see above), we can reasonably associate this mica group to the Beauvoir greisen alteration. To conclude, all genetic links highlighted by the trace element chemistry are supported by geochronological data, validating the multivariate analytical protocol.

5.1.2. Typical signature enrichment for each mica-forming episode.

Combining petrological observations, multivariate analysis and chronological data, we have clustered the different mica groups as a function of the different mineralizing episodes, in order to characterize each magmatic and hydrothermal episode by their specific trace-element concentration (Fig. 11). Micas from the Colettes granite are characterized by high Ti, Nb, Ta, Ge contents, are slightly enriched in W, and have a medium Sn and low Rb, Sr, Cs and Ba contents. Igneous micas from the Beauvoir magmatic episode are characterized by high Rb, Nb, Ta, W contents, intermediate Cs and Ge contents, and low Ti, Sr (bdl), Sn, and Ba. Zinnwaldite (1) is considered as originating from the La Bosse stockwork formation. Although constrains on this episode are weak due to the several metamorphic and magmatic/hydrothermal episodes that affected the area, zinnwaldite (1) records a singular signature, suggesting a specific hydrothermal event. Notably, Ti, Cs, Rb and Ba are relatively enriched, Nb, Ta, Ge and Sr are present in intermediate proportions, while Sn and W are relatively depleted. The topazification episode led to crystallization of micas that incorporated high Ti, Sr, Ba, intermediate Nb, Ge, Sn W, and low Rb, Cs, Ta contents. Lepidolite (4) from the orthomagmatic Beauvoir episode is characterized by high Rb, Cs, Ta, Sn, Ba and W contents, intermediate Ti, Nb and Ge, and low Sr (bdl) contents. Micas precipitating from the Beauvoir greisen fluid display high Sn, intermediate Rb, Sr, Ba, and low Ti, Nb, Cs, Ta, Ge, W contents, although some of these elements, i.e., Ta, Sr, Sn, vary widely.

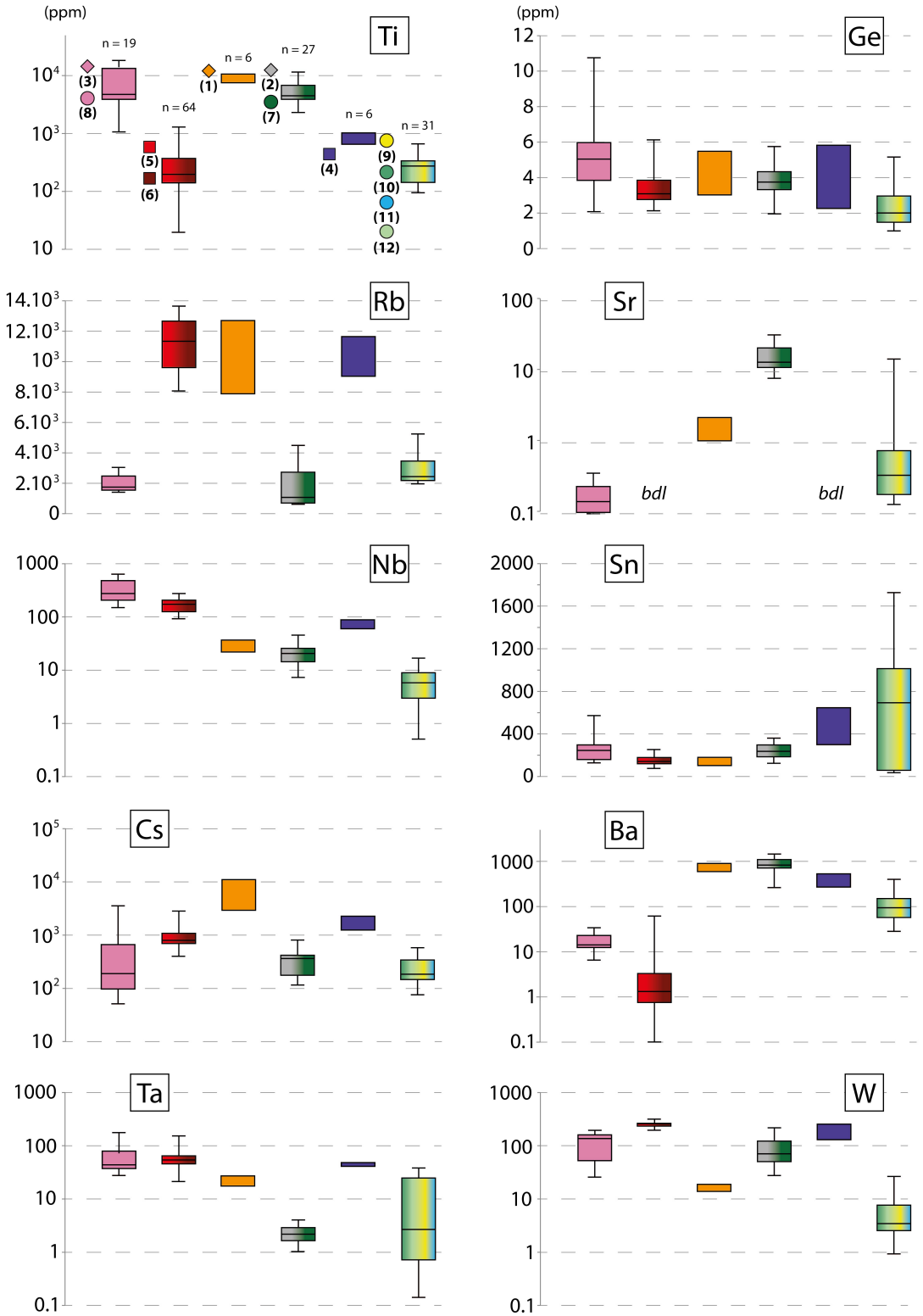

Fig. 11. Boxplot diagrams depicting trace-element data for the petrographic mica groups (cf., Fig. 5 for legend), clustered according to igneous and hydrothermal episodes recognized in the Echassières district by a combination of petrological, geochronological and trace-element data. The boxes for zinnwaldite (1, orange) and lepidolite (4, violet) are formed only by minimum and maximum values due to a low number of analyses.

5.1.3. Global implication.

It was expected that incorporation of trace elements in micas would be dictated mostly by the nature of the mica species (i.e., major elements) and the corresponding trace element partition coefficients (e.g.,

Stepanov et al., 2014). However, the results of the multivariate analysis reveal groups that are heterogeneous in terms of major compositions, but share a similar origin/source. This implies that trace element incorporation in micas is in fact dictated mainly by the chemistry of the melt or fluid from which they precipitate. Different mica species can therefore be compared and their trace-element signatures used as a powerful tool to unravel intricate paragenesis, ranging from magmatic to hydrothermal conditions, of which the polyphased ore system investigated herein is one example. With sufficient samples, it is even possible to trace the evolution of a fluid that underwent cooling and mixing, leading to significant chemical changes, by recognizing different snapshots of its passage in hydrothermal mineral assemblages that could otherwise appear petrographically unrelated (e.g., evolution path of Beauvoir greisen fluid; yellow arrow on Fig. 12). Moreover, orthomagmatic micas can display a roughly similar chemistry to that of primary igneous micas, where only very few elements vary (e.g. Beauvoir magmatic/hydrothermal path, red arrow on Fig. 12). It can be deduced that the trace chemistry of an orthomagmatic fluid remains largely dominated by the chemical nature of the melt that sourced it, providing an opportunity to use the trace chemistry of alteration mica as a proxy for strongly evolved rare-metal granite. It should be kept in mind that these concentrations can vary within the order of magnitude scale, given that partition coefficient between fluid and melt as well as between various micas and the crystallizing medium are a function of different parameters. Nevertheless, the chemical variation of magmas and fluids from radically different sources will vary to a much wider scale (several orders of magnitude for key elements) thus allowing definition of specific signatures. Similarly to major element chemistry, petrographic features, such as mineral texture and color, can vary widely during a single mineralizing episode, remaining poor indicators for deciphering polyphased mineralization. Moreover, considering that Ar-Ar dating of mica is often partially, if not entirely, reset in these complex systems and does not reflect ore deposition age (e.g., Zhang et al., 2017; Tichomirowa et al., 2019; Legros et al., 2020; Carocci et al., 2020), trace-element signature determination coupled to multivariate analysis could be a powerful alternative to provide relative chronology and distinguish successive hydrothermal events.

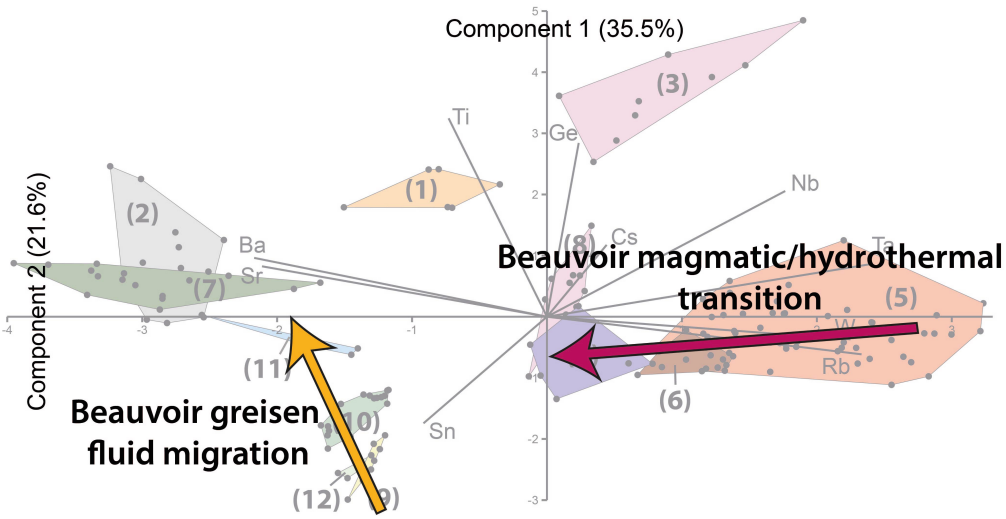

Fig. 12 superposition of Beauvoir magmatic/hydrothermal transition and Beauvoir greisen fluid transport trends on PCA (component 1 and 2) from Figure 9. The Beauvoir magmatic hydrothermal transition is characterized by enrichment in Sn, Ba, Sr and depletion in Nb, Ta, W, Rb. Concerning the greisen fluid, Ba, Sr and Ti increase all along the transport, on the contrary of Sn which drastically decreases, among others.

5.2. Genetic considerations on the Colettes/Beauvoir system

5.2.1. Magmatic evolution of the Colettes and Beauvoir granites.

Considering that the Beauvoir granite is one of the most evolved peraluminous melt occurrences known (Linnen and Cuney, 2005), the exceptional enrichment in several trace elements in its primary igneous mica (5) is not surprising. On the other hand, the strong enrichment in some elements (Nb, Ta, W, Sn) measured in zinnwaldite and muscovite from the Colettes granite was unexpected. The amount of several of these elements is comparable to those measured in micas from a number of RMG (e.g., Li et al., 2015), indicating that the Colettes granite, albeit barren of mineralization *per se*, is probably related to the evolution of the Beauvoir granite, as also suggested by their contemporaneous emplacements (Monnier et al., 2021a and references therein). Most RMG occurrences that have been drilled at depth consist of a well delimited root of zinnwaldite or two-micas granite, and an apex of albite-lepidolite/zinnwaldite granite (e.g., Yashan, Cínovec and Panasqueira granites, respectively, Li et al., 2015, Breiter et al., 2017, and Marignac et al., 2020). In contrast, deep drilling of the Beauvoir RMG revealed only the presence of the schist host rock at its base. Thus, if we assume that the Colettes granite represents the equivalent of a barren granitic root for other RMG, we could conclude that the final crystallization of the Beauvoir and Colettes granites took place

after melt segregation and transport of the resulting melts, contrasting with emplacement models proposed for most RMG, worldwide. The magmatic source of Beauvoir and Colettes granites could be related to the porphyry enclave (Monnier et al., 2018) commonly found in the root of the Beauvoir granite. The less evolved nature of the Colettes magma compared to Beauvoir is not recorded by the rare element signatures of micas. Indeed, the contents of some elements are higher in micas from Colettes than Beauvoir, i.e., Nb, Ta, and Sn in both muscovite (8) and zinnwaldite (3).

Concerning the Beauvoir intrusion, variations in the content of some elements in lepidolite (5) provide a nice record of its magmatic evolution, from the least evolved unit 3, at the root of the granite, to the highly evolved apex, illustrating a vertical zonation through the Beauvoir intrusion (Fig. 13). Surprisingly, however, in the least evolved unit, lepidolite concentrates the highest amounts of some incompatible elements such as Nb and Sn, possibly because of the relatively low abundance of competitor ore minerals in this unit. Conversely, lepidolite from the more evolved magmatic facies is enriched in Ba, Mg and Na, which mostly reflects the input of exotic fluids during the last magmatic stage, as also documented by isotopic evidence (Fouillac and Rossi, 1991) and whole-rock chemistry (Raimbault et al., 1995).

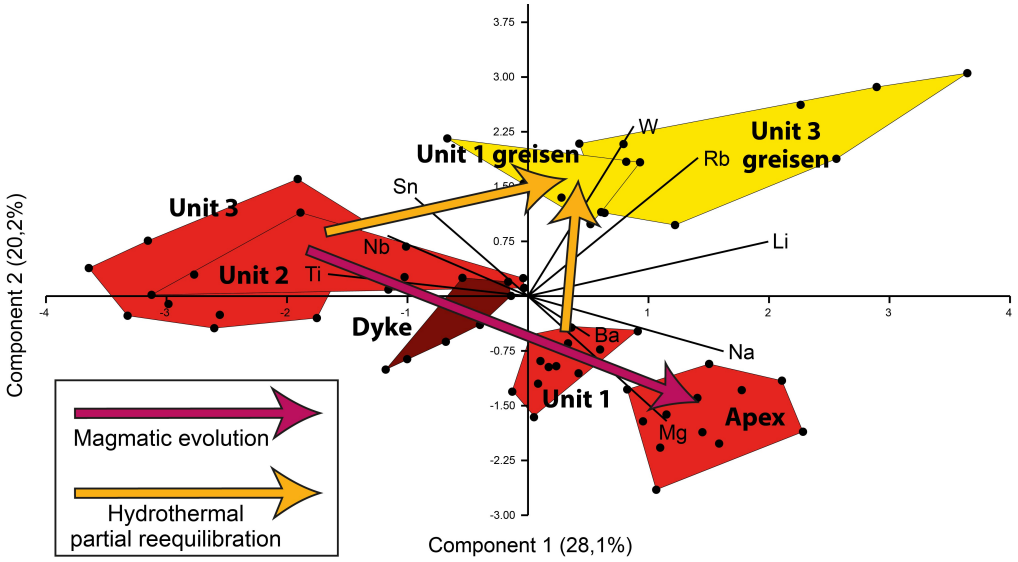

Fig. 13. PCA diagram projecting components 1 and 2 for LA-ICP-MS data for a selected panel of elements (Li, Na, Mg, Ti, Rb, Nb, Sn, Ba, W) from all igneous lepidolite analyzed in this study.

The unprecedented concentration of W in igneous micas (5) recorded in this study signifies that an important quantity of igneous-sourced W remained in the Beauvoir granite during crystallization. Also, although igneous columbo-tantalite and pyrochlore host significant amounts of W (ca. 1 and 2 wt % of

555 WO_3, respectively, see Table A3 in Appendices), a simple model based on micas chemistry, modal
556 composition and whole rock values (ca. 35 ppm; Raimbault et al., 1995) indicates that the majority of the
557 Beauvoir granite W stock is hosted in lepidolite (Fig. 14). This result has far-reaching implications:
558 incorporation of significant concentrations of W in lepidolite from the Beauvoir granite disagrees with the
559 generally accepted paradigm that W fractionates into the fluid during fluid/melt interaction (Keppler et al.,
560 1991; Zajacz et al., 2008). Furthermore, incorporation of W in igneous micas can potentially inhibit
561 subsequent hydrothermal W mineralization. In comparison, at Cínovec, where important hydrothermal W
562 mineralization occurs, magmatic zinnwaldite contains only between about 3 to 30% of the total W stock
563 (Breiter et al., 2019). As expected, Li and Rb behave similarly, i.e., they are hosted in trioctahedral micas
564 (Tischendorf et al., 2001) while Ta, and especially Sn, are mainly hosted in other minerals, undoubtedly
565 columbo-tantalite and cassiterite, respectively.

566 Only negligible variations in lepidolite Nb/Ta ratios were observed from the lowermost unit to the apex of
567 the granite. These range from a minimum of 2.7 in unit 2 to a maximum of 3.8 in unit 3. Still, these values
568 are markedly higher than the whole-rock Nb/Ta ratios (<1 in the upper units and ~1 in unit 3; Raimbault et
569 al., 1995), indicating that columbo-tantalite or pyrochlore should be expected to be an important stock of
570 Ta at Beauvoir, as in other extremely evolved melts. This process, and specifically the role of mica
571 crystallization in the decrease of the Nb/Ta ratio in granitic melts, has been thoroughly investigated by
572 Stepanov et al. (2014).

573

574 *5.2.2. Hydrothermal alteration: orthomagmatic, hybrid or exotic fluid origin.*

575 The source of fluids that precipitate W and Sn is a highly debated topic with implications for the
576 comprehension and recognition of these deposits. The Beauvoir granite and its proximal host rock
577 experienced several types of alterations (Monnier et al., 2018, 2019, 2020, 2021a), to variable intensities.
578 In chronological order, these consist mainly of: orthomagmatic alteration (localized), alkali alteration
579 (localized), and greisenization (widespread). Long after these events, a widespread kaolinisation affected
580 the whole area. As mentioned above, the chemical signature of lepidolite (4) that crystallizes from the

orthomagmatic fluid is strongly similar to that of igneous lepidolite, suggesting that the orthomagmatic fluid and the Beauvoir melt have similar trace-element signatures. One can also deduce that the orthomagmatic fluid was not subject to drastic chemical variations before precipitation of lepidolite (4) and, by extrapolation, did not undergo mixing nor fluid immiscibility or segregation, at least at an early stage. This also implies that a massive hydrothermal precipitation of ore minerals before formation of this lepidolite (4) is to be excluded, as it would have drastically decreased the contents of Nb, Ta, W and Sn in micas. Conversely, micas precipitating from the greisen episode display a markedly different signature than that of igneous lepidolite. Such disparity can be explained by repeated boiling episodes of the greisen fluid and its mixing with other fluids. This, as evidenced by Monnier et al. (2020), led to phase segregation and dissolution of igneous minerals with coeval muscovite precipitation, efficiently altering the pristine signature of the fluid. In the Echassières district, Sr and Ba incorporation in micas correlates roughly with the distance from the magmatic source, reflecting a potential contamination from the schist during fluid-rock interaction. Similar findings are also reported by Codeço et al. (2021) at Panasqueira (Portugal) for both elements, and by Legros et al. (2018) for Ba at Jiangxi (China; Sr was not analyzed). Consequently, variations in the concentration of these elements in mica could be used as a proxy for the distance traveled by a fluid from its granitic source. Monitoring in parallel distal hydrothermal micas for their content in W, Sn, Nb-Ta, should prove mica trace-element signature as a robust tool for targeting potentially mineralized granitic body.

5.2.3. Metals behavior during greisen alteration of the Beauvoir granite.

Recently, an experimental study by Schmidt et al. (2020) highlighted the contrasting behavior of W and Sn during melt/fluid partitioning, replicating the distal hydrothermal deposition of W and the conservation of Sn in the magma at late stages of crystallization, as is generally inferred for natural systems. Nevertheless, their study indicates that W preferentially fractionates in the melt phase for strongly peraluminous compositions, as is the case for the Beauvoir granite. At first sight, this remarkable result contradicts the common observation that, in some peraluminous RMG, most cassiterite is igneous while wolframite crystallizes in quartz veins (e.g., Argemela, Michaud et al., 2020; Abu Dabbab, Zoheir et al., 2020; Beauvoir,

607 this study). Moreover, it has been shown experimentally that wolframite cannot reach saturation in a
608 halogen-rich melt above 500 °C (Che et al., 2013), implying that, in these peraluminous melts, W is hosted
609 in (an) igneous phase(s) other than wolframite. In the case of the Beauvoir granite, and likely for other
610 peraluminous RMG, igneous mica incorporates significant quantities of W, and fluid exsolution during
611 magmatic crystallization will not lead to W mineralization, in agreement with the high melt/fluid
612 partitioning for W highlighted by Schmidt et al. (2020). Monnier et al. (2020) demonstrated that, in the
613 Echassières district, the mineralization of wolframite *c,* found outside of the Beauvoir granite, clearly
614 postdated crystallization of the latter. They also showed that the tungsten could not have derived from the
615 early orthomagmatic fluid. If its source is unclear, the most likely hypothesis would be remobilization
616 during greisen alteration. Dissolution of the early wolframite generations (*a* and *b*) may have provided the
617 W to form wolframite *c*, but textural evidences for replacement of early wolframite generations are scarce
618 at best and do not support this postulate. In the light of the findings discussed so far, it would seem
619 worthwhile to seek answers by investigating the composition of associated mica groups. Surprisingly, W
620 concentrations measured in greisen muscovite from Beauvoir greisen are particularly low compared to
621 igneous lepidolite. Indeed, our data (Fig. 14) indicate that lepidolite stocked the majority of the W
622 contained in the Beauvoir

granite, as it is generally the case for white micas in peraluminous granites (e.g, Neves, 1997). It is therefore a likely scenario that alteration of lepidolite into muscovite, occurring during greisen alteration of the granitic stock, allowed remobilization of important quantities of W, which did not incorporate in the newly formed, W-depleted, muscovite. A quick calculation can provide an estimate of the mass of W released to the greisen fluid (Fig. 15, see the caption for more details). For a volume of ca. 5 % of greisen altered granite, the quantity of W released corresponds to 5000 T of WO_3, i.e., an amount significantly higher than that of the W stock assessed for the Mazet veins prospect, where most wolframite c was found (Aubert, 1969). This result is provocative and implies that if a similar/higher volume of a rare-metal granite with an analogous chemistry to Beauvoir were to be altered to a similar/higher intensity, the greisen fluid could remobilize a sufficient amount of W to form a major deposit. A similar approach, using trace element differences between igneous and replacing hydrothermal mica, reached the same conclusions for the Cínovec granite (**Johan** et al., 2012), though these are subject of debate (**Breiter** et al.,).

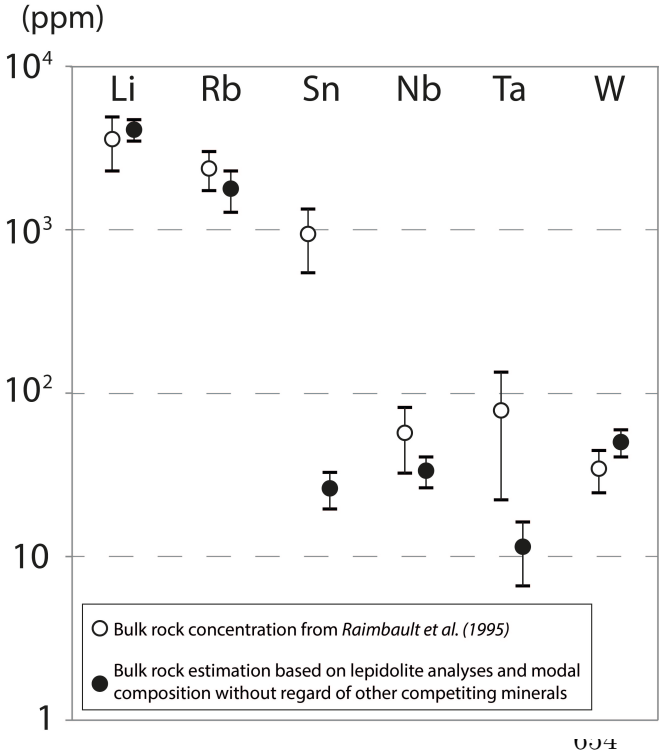

Fig. 14. Comparison between bulk rock concentrations in rare metals and their estimated stock in micas for the Beauvoir granite. The latter value was obtained combining the LA-ICP-MS analyses in this study with modal mica compositions. Mean bulk rock data was calculated from concentrations measured in drill core by listed in Raimbault et al. (1995). Altered samples, uncommon rock facies and samples displaying a high number of outlier concentrations were not considered. Intervals used are (in meters below surface): Unit 1: -129.4; -208.9; -269.7; -354.6. Unit 2: -445.2; -507.6; -517.4; -521.6; -561.9; -632.7; -656.8; -716.6. Unit 3: -751.1; -771.0; 785.6. Error bars correspond to the standard deviations of lepidolite and whole rock analyses. The similar bulk and mica Li and Rb stocks displayed validate this approach, considering the fact that these elements occur mostly in mica.

In a few greisen samples, igneous lepidolite relicts were relatively well preserved (Fig. 2.C). Their composition differs from that of the igneous lepidolite population from unaltered samples, which has a

relatively consistent chemistry, by an increase in Rb, Li and W (Fig. 13). These chemical changes are clearly minor in regard of the differences segregating the mica groups sourced by distinct magma or fluids. Nevertheless, this observation suggests a partial re-equilibration of the lepidolite relicts during greisen fluid percolation, confirming its particularly high W content. Other similar outcomes, such as the significant increase of W concentration monitored in hydrothermal pyrochlore and columbo-tantalite (ca. 3 wt % of WO_3) compared to the igneous species (Table A3), confirm the global W enrichment in the Beauvoir greisen fluid. We assume that this enrichment is mainly due to release of W during alteration of lepidolite into muscovite, as discussed in section 5.2.3 (Fig. 15). It follows that the conditions necessary for the breakdown of lepidolite, or other W-rich micas, are key factors for releasing potential economic quantities of this metal. Observations at a global scale reveal that particularly evolved peraluminous granites have a better chance of developing quartz vein-hosted W mineralization. Yet, the experimental investigation of Schmidt et al. (2020) indicates that, in strongly peraluminous systems, most of the W is retained in the magma throughout granite crystallization. Their results are inconsistent with precipitation of abundant hydrothermal wolframite, given that a fluid exsolving from a crystallizing granite – the generally evoked process to account for these mineralizations – would probably carry only little W in solution. An explanation to this paradox would be that, sometime after crystallization of the granite, metals are release into the fluid that is altering the W-bearing igneous minerals. Such a fluid could be a moderate-temperature evolved greisen fluid, similar to what we have documented at Beauvoir (Monnier et al., 2020).

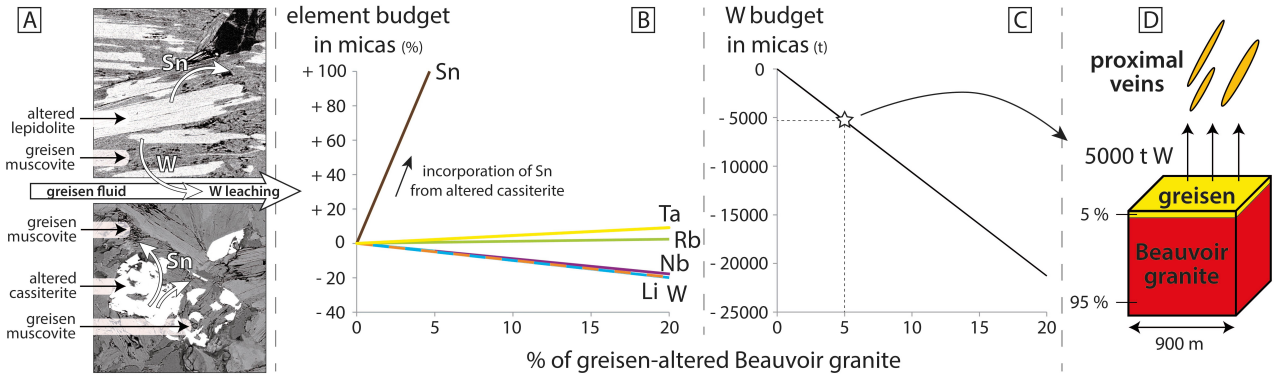

Fig. 15. A conceptual model summarizing the transferring process of metals from the source rock to the depositional site via fluid transport. [A]: During greisen alteration, primary lepidolite and cassiterite are replaced by muscovite. Tungsten in lepidolite is leached by the fluid while Sn from both altered minerals is incorporated in newly formed muscovite. [B]: Based on modal proportions and average compositions of micas from this study, this diagram monitors the estimated budget of metals in micas during greisen alteration of the Beauvoir granite. The steep increase of the Sn budget in mica is only possible for a case where Sn is provided by

(an) other source(s), such as cassiterite; if all Sn were to come from lepidolite, even if entirely incorporated in muscovite (100%), there would be a steady state in the total budget (0%), as is approximately the case for Rb and Ta. Conversely, the negative slopes for Nb, Li and W indicate that these elements are not incorporated in greisen mica. This may imply that they are fractionated into the fluid, although Nb-Ta behavior is also constrained by formation/dissolution of columbo-tantalite and pyrochlore. [C]: This diagram focusses on the W budget (in metric tons) in mica, for the same amount of rock altered as in B. It indicates that, for 5% altered granite, 5.10^3 t of tungsten are removed from the altered rock. This amount of metal is transported by the fluid and reprecipitated in form of wolframite in proximal veins [D]. The model considers that lepidolite is the main primary host of W (cf., Fig. 14) and that secondary minerals other than wolframite do not incorporate significant amounts of this metal. In this simulation, unaltered granite is considered to contain 18 % modal lepidolite and have a whole-rock average density of 2.6, for a total granite volume of 7.29 x 10^8 m^3. The modal proportion of greisen muscovite (9) is 66%, with average bulk density of 2,3 for the greisen. The simulation assumes that the altered portion of the primary rock is entirely transformed to greisen.

Cassiterite is the main Sn-bearing igneous mineral in the Beauvoir granite (Fig. 15). Considering the fact that cassiterite was strongly altered during greisen alteration (Wang, 1988; Monnier et al., 2019), it could be expected that, as was the case for W, Sn should undergo important remobilization away from the granite during alteration by the greisen fluids (e.g., Linnen and Cuney, 2004; Chen et al., 2019). However, only minor cassiterite occurs outside of the granite, far too little to account for the high quantity of igneous cassiterite altered. However, greisen muscovite (9) that replaced igneous minerals contains exceptional Sn contents, largely superior to the amount recorded in igneous lepidolite. Also, the modal amount of muscovite in greisen is much higher than that of lepidolite in the fresh granite. It is thus quite likely that Sn released from cassiterite and lepidolite during alteration was mostly trapped in greisen muscovite, thus inhibiting Sn migration outside of the Beauvoir granite. A rough estimate of the muscovite capacity to stock Sn issued from altered cassiterite can be obtained using the same simple model used above to calculate W remobilization. An alteration of ca. 5 % of the granite volume would lead to incorporation of ca. 50,000 metric tons of Sn in muscovite. This represents an important amount, considering that the estimated Sn stock for the 300 upper meters of the granite was of ca. 150,000 metric tons (Cuney et al., 1992). Niobium, Ta, Li and Rb form two element couples with similar behavior in geological systems, so that they are commonly incorporated in the same minerals in evolved peraluminous granites, i.e., columbo-tantalite for Nb-Ta and micas for Li-Rb. The latter pair are particularly enriched in lepidolite from the Beauvoir granite (5), however, only Rb was efficiently incorporated in the greisen muscovite (9), inducing a roughly steady stock of Rb in Beauvoir micas during greisen alteration. Lithium, on the other hand, is very low in greisen muscovite, suggesting that, in contrast to Rb, it remained mostly in solution after lepidolite dissolution.

715 Again, if we use the above model, altering 5 % of Beauvoir granite to greisen and considering that
716 muscovite was the only mineral efficiently incorporating Li, would induce an estimate of ca. 4. 10^5 T of Li to
717 be removed from the granite. This observation confirms that the Li anomaly marking a well-defined
718 geochemical halo in the schist around the Beauvoir granite (Cuney et al., 1992) can be related to greisen
719 alteration of the granite. Similarly to Li and Rb, Nb and Ta were unequally incorporated in greisen
720 muscovite (9). The Nb/Ta ratio is lower in greisen muscovite then in igneous lepidolite, suggesting that the
721 solubility of Nb species exceeds that of Ta in the greisen fluid. A similar process has been proposed for
722 zoned micas of the Dahutang deposit (Yin et al., 2020), confirming that Nb has a higher affinity for greisen
723 fluids than Ta does. Nevertheless, in the Beauvoir granite, columbo-tantalite and pyrochlore seem to be
724 major reservoirs for Ta and possibly Nb (Fig. 14) both at the magmatic and greisen stages, complicating the
725 interpretation of variations in Nb and Ta concentrations in micas. It would therefore be advisable to
726 envisage a paired investigation on these ore minerals in the Echassières district, and, in a more general
727 manner, other occurrences elsewhere.

728 *5.2.4. Transport of Sn, W, Nb, Ta, Li and Rb during the greisen episode.*

729 The various micas that crystallized from the greisen fluid form a group with a coherent chemical signature
730 that differentiates them from the other mica groups. Nonetheless, several minor differences do occur in
731 each subgroup (Fig. 9 and 10, Table 3 and 4), particularly as a function of the distance from the Beauvoir
732 granite. These differences illustrate the ability of the greisen fluid to transport some of these key elements.
733 They also provide a vectoring tool, assuming than the increased content of metals that were strongly
734 remobilized from the Beauvoir granite during greisen alteration (i.e., Li, W and possibly Nb) reflects their
735 respective decrease in solubility in the greisen fluid as the latter evolves during migration. On the contrary,
736 the contents of elements that mostly remained in the granite after greisen alteration (i.e., Rb, Sn and Ta)
737 decrease markedly in micas with distance from the granite, corroborating that the fluid is not able to
738 mobilize these metals (Fig. 16). These observations are consistent with the estimated metal budget in
739 Beauvoir micas during greisen alteration: rare elements that strongly incorporated in greisen muscovite (9)
740 are very low in muscovite (11) from the Suchot vein (located outside the granite), while elements that were

741 easily remobilized in the greisen fluid are relatively concentrated in micas outside of the granite. This
742 process led to the occurrence of wolframite *c* outside of the Beauvoir granite (increase of W in micas after
743 fluid transport) while cassiterite is scarce in these same rocks (decrease of Sn in micas after fluid transport).
744 The above observations confirm that the mica trace-element signatures provide a suitable record for ore
745 metal remobilization and transport. Additional studies involving ore element mobility in greisen fluids are
746 clearly needed in order to better constrain the genesis of greisen-related deposits, globally.

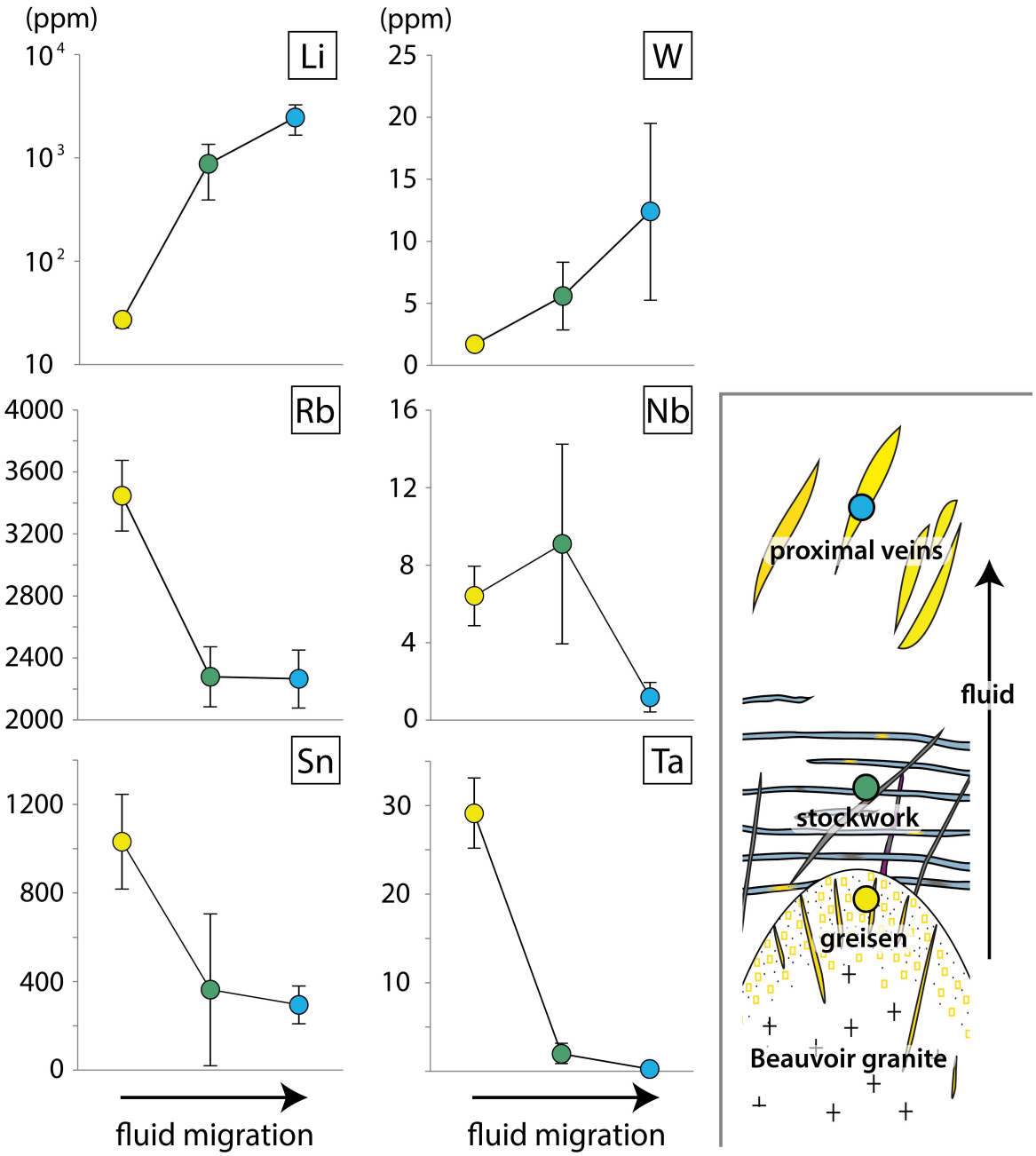

747 *Fig. 16. On the left-hand side are depicted mean and standard deviation concentrations of a number*
748 *of critical metals analyzed in the greisen muscovite from granite, stockwork and proximal veins*
749 *(respectively, yellow, green and blue circles in the sketch to the right). The data trends record the*
750 *evolution of the fluid during transport of these metals (fluid migration).*

In summary, it is clear that crystallization and dissolution of micas played a key role in determining the fate of at least some critical metals throughout the magmatic/hydrothermal evolution of the Beauvoir granitic system. In particular, remobilization of W, Sn, Li and Rb was strongly influenced by dissolution of igneous lepidolite and crystallization of greisen muscovite, while the process of Nb and Ta remobilization seems more complex, possibly controlled by the behavior of columbo-tantalite and pyrochlore precipitation/alteration. Metal incorporation into greisen muscovite (W-poor and Sn-rich) controlled the leaching of W away from the granite, while the Sn remobilized from cassiterite remained sequestered in the granite (Table 5). A similar process (alteration of metal-enriched igneous mica) was evoked as the possible mechanism for the origin of the Nb-Ta hydrothermal mineralization and peripheral W vein formation in the Yashan granite (China, Li et al., 2015). This process must therefore be kept in mind when investigating greisen-related W deposits, particularly those associated to RMG peraluminous magmatism.

Metal	Main igneous mineral host	Behavior during greisen alteration	Fate after transport away from the granite
W	Lepidolite	Mainly remobilized by fluids	Wolframite c
Sn	Cassiterite	Mostly incorporated in greisen muscovite	Limited occurrence of cassiterite
Li	Lepidolite	Mainly remobilized by fluids	Incorporation in metamorphic mica
Rb	Lepidolite	Mostly incorporated in greisen muscovite	Limited occurrence
Nb	Columbo-tantalite (lepidolite)	Mainly remobilized by fluids	Lack of mineralization evidence. Incorporation in rutile or micas ?
Ta	Columbo-tantalite, pyrochlore	Mostly incorporated in hydrothermal pyrochlore	Limited occurrence

Table 5: Ore metal behaviors during Beauvoir greisen alteration.

6. Conclusions

A multivariate statistical approach on trace element data obtained from micas by LA-ICP-MS provides important insights on the magmatic/hydrothermal processes that can lead to ore accumulation. Key findings of this study are hither condensed:

- Micas chemical signatures provide a direct vector to W, Sn, Nb-Ta mineralizations.

- During a single hydrothermal episode, micas precipitating in different hydrothermal parageneses maintain a roughly similar trace-element signature. This also applies to micas formed within (in the quartz or topaz matrix) and outside a vein (in alteration halo). It follows that fluid-rock interaction has a low impact on the chemical compositions of newly formed micas.
- The trace element chemistry of micas can be used as a powerful tool to differentiate or link different alteration parageneses, more efficient than major elements and/or petrographic features. It can also relate distal dykes to a main magmatic body.
- Igneous micas can host significant concentrations of W and Sn which can be remobilized during hydrothermal alteration to potentially form ore deposit. Conversely, hydrothermal mica precipitation can inhibit ore formation by incorporating substantial quantities of metals.

Acknowledgments

We would like to thank the BRGM (French Geological Survey), the CNRS (French National Center for Scientific Research) and the University of Toulouse for providing financial support to this study. We are grateful to IMERIS for allowing access to the Beauvoir quarry for field work and sampling. . We are indebted to Chemical Geology reviewers Huan Li and Karel Breiter for their sharp insights that have contributed to the quality of the final manuscript. We would like to extend a particular mention to Karel, who has followed our team's investigations on RMG for several years now, and has never failed to spot the slightest inconsistency that we may have overlooked.

Appendices

Appendices contains the following research data:

Table A1: EPMA analyses of micas from Echassières district (in wt. %)

Table A2: LA-ICP-MS analyses of micas from Echassières district (in ppm)

Table A3: EPMA analyses of columbo-tantalite and pyrochlore from the Beauvoir granite (in wt. %)

References

Adam, J., & Green, T. (2006). Trace element partitioning between mica-and amphibole-bearing garnet lherzolite and hydrous basanitic melt: 1. Experimental results and the investigation of controls on partitioning behaviour. Contributions to Mineralogy and Petrology, 152(1), 1-17. https://doi.org/10.1007/s00410-006-0085-4

Anderson, M. J. (2001). A new method for non-parametric multivariate analysis of variance. Austral ecology, 26(1), 32-46. https://doi.org/10.1111/j.1442-9993.2001.01070.pp.x

Aubert, G. (1969). in French. Les coupoles granitiques de Montebras et d'Échassières: (Massif Central français) et la genèse de leurs minéralisations en étain, lithium, tungstène et béryllium. Paris, BRGM press, BRGM mémoires 46, 349 p.

Aubert, G., & Contamine, L. (1958). In french. Concession d'antimoine de Nades (Allier). Rapport d'étude. BRGM report.

Azadbakht, Z., & Lentz, D. R. (2020). High-resolution LA-ICP-MS trace-element mapping of magmatic biotite: A new approach for studying syn-to post-magmatic evolution. The Canadian Mineralogist, 58(3), 293-311. https://doi.org/10.3749/canmin.1900101

Azadbakht, Z., Lentz, D. R., McFarlane, C. R., & Whalen, J. B. (2020). Using magmatic biotite chemistry to differentiate barren and mineralized Silurian–Devonian granitoids of New Brunswick, Canada. Contributions to Mineralogy and Petrology, 175(7), 1-24. https://doi.org/10.1007/s00410-020-01703-2

Bebout, G. E., Bebout, A. E., & Graham, C. M. (2007). Cycling of B, Li, and LILE (K, Cs, Rb, Ba, Sr) into subduction zones: SIMS evidence from micas in high-P/T metasedimentary rocks. Chemical Geology, 239(3-4), 284-304. https://doi.org/10.1016/j.chemgeo.2006.10.016

Beswick, A. E. (1973). An experimental study of alkali metal distributions in feldspars and micas. Geochimica et Cosmochimica Acta, 37(2), 183-208. https://doi.org/10.1016/0016-7037(73)90128-2

Bray, J. R., & Curtis, J. T. (1957). An ordination of the upland forest communities of southern Wisconsin. Ecological monographs, 27(4), 326-349.

817 Breiter, K., Vaňková, M., Galiová, M. V., Korbelová, Z., & Kanický, V. (2017). Lithium and trace-element
818 concentrations in trioctahedral micas from granites of different geochemical types measured via laser
819 ablation ICP-MS. Mineralogical Magazine, 81(1), 15-33. https://doi.org/10.1180/minmag.2016.080.137
820 Breiter, K., Hložková, M., Korbelová, Z., & Galiová, M. V. (2019). Diversity of lithium mica compositions in
821 mineralized granite–greisen system: Cínovec Li-Sn-W deposit, Erzgebirge. Ore Geology Reviews, 106, 12-27.
822 https://doi.org/10.1016/j.oregeorev.2019.01.013
823 Brigatti, MF, Guggenheim S. (2002) Mica crystal chemistry and the influence of pressure, temperature, and
824 solid solution on atomistic models. Reviews in Mineralogy and Geochemistry 46.1, 1-97.
825 Carocci, E., Marignac, C., Cathelineau, M., Truche, L., Poujol, M., Boiron, M. C., & Pinto, F. (2020). Incipient
826 wolframite deposition at Panasqueira (Portugal): W-rutile and tourmaline compositions as proxies for early
827 fluid composition. Economic Geology.
828 Cesare, B., Satish-Kumar, M., Cruciani, G., Pocker, S., & Nodari, L. (2008). Mineral chemistry of Ti-rich
829 biotite from pegmatite and metapelitic granulites of the Kerala Khondalite Belt (southeast India): Petrology
830 and further insight into titanium substitutions. American Mineralogist, 93(2-3), 327-338.
831 https://doi.org/10.2138/am.2008.2579
832 Che, X. D., Linnen, R. L., Wang, R. C., Aseri, A., & Thibault, Y. (2013). Tungsten solubility in evolved granitic
833 melts: An evaluation of magmatic wolframite. Geochimica et Cosmochimica Acta, 106, 84-98.
834 https://doi.org/10.1016/j.gca.2012.12.007
835 Chen, G., Gao, J., Lu, J., & Zhang, R. (2020). In situ LA-ICP-MS analyses of mica and wolframite from the
836 Maoping tungsten deposit, southern Jiangxi, China. Acta Geochimica, 1-19.
837 https://doi.org/10.1007/s11631-020-00423-5
838 Codeço, M. S., Weis, P., Trumbull, R. B., Van Hinsberg, V., Pinto, F., Lecumberri-Sanchez, P., & Schleicher, A.
839 M. (2021). The imprint of hydrothermal fluids on trace-element contents in white mica and tourmaline
840 from the Panasqueira W–Sn–Cu deposit, Portugal. Mineralium Deposita. https://doi.org/10.1007/s00126-
841 020-00984-8

842 Cuney, M., Marignac, C., & Weisbrod, A. (1992). The Beauvoir topaz-lepidolite albite granite (Massif
843 Central, France); the disseminated magmatic Sn-Li-Ta-Nb-Be mineralization. Economic Geology, 87(7),
844 1766-1794. https://doi.org/10.2113/gsecongeo.87.7.1766 https://doi.org/10.2113/gsecongeo.87.7.1766

Do Couto, D., Faure, M., Augier, R., Cocherie, A., Rossi, P., Li, X. H., & Lin, W. (2016). Monazite U– Th– Pb EPMA and zircon U–Pb SIMS chronological constraints on the tectonic, metamorphic, and thermal events in the inner part of the Variscan orogen, example from the Sioule series, French Massif Central. International Journal of Earth Sciences, 105(2), 557-579. https://doi.org/10.1007/s00531-015-1184-0

Faure, M., Monié, P., Pin, C., Maluski, H., & Leloix, C. (2002). Late Visean thermal event in the northern part of the French Massif Central: new 40 Ar/39 Ar and Rb–Sr isotopic constraints on the Hercynian syn-orogenic extension. International Journal of Earth Sciences, 91(1), 53-75. https://doi.org/10.1007/s005310100202

Foster, M. D. (1960). Layer charge relations in the dioctahedral and trioctahedral micas. American Mineralogist: Journal of Earth and Planetary Materials, 45(3-4), 383-398.

Fouillac, A. M., & Rossi, P. (1991). Near-solidus delta 18 O depletion in a Ta-Nb-bearing albite granite; the Beauvoir Granite, France. Economic Geology, 86(8), 1704-1720. https://doi.org/10.2113/gsecongeo.86.8.1704

Gao, X., Zhou, Z., Breiter, K., Ouyang, H., & Liu, J. (2019). Ore-formation mechanism of the Weilasituo tin–polymetallic deposit, NE China: Constraints from bulk-rock and mica chemistry, He–Ar isotopes, and Re–Os dating. Ore Geology Reviews, 109, 163-183. https://doi.org/10.1016/j.oregeorev.2019.04.007

Guimarães, F. S., de Oliveira, A. L. R., Amorim, L. E. D., Rios, F. J., Lehmann, B., Hernández, C. R., & Moraes, R. (2021). Lithium-mica composition as pathfinder and recorder of Grenvillian-age greisenization, Rondonia Tin Province, Brazil. Geochemistry, 125737. https://doi.org/10.1016/j.chemer.2020.125737

Han, J., Chen, H., Hollings, P., Wang, J., Zhang, D., Zhang, L., ... & Ai, Y. (2021). Efficient enrichment of Rb during the magmatic-hydrothermal transition in a highly evolved granitic system: Implications from mica chemistry of the Tiantangshan Rb-Sn-W deposit. Chemical Geology, 560, 120020. https://doi.org/10.1016/j.chemgeo.2020.120020

Hammer, Ø., Harper, D. A., & Ryan, P. D. (2001). PAST: Paleontological statistics software package for education and data analysis. Palaeontologia electronica, 4(1), 9.

870 Harlaux, M., Mercadier, J., Bonzi, W. M. E., Kremer, V., Marignac, C., & Cuney, M. (2017). Geochemical
871 signature of magmatic-hydrothermal fluids exsolved from the Beauvoir rare-metal granite (Massif Central,
872 France): Insights from LA-ICPMS analysis of primary fluid inclusions. Geofluids, 2017, 1-25.
873 https://doi.org/10.1155/2017/1925817
874 Harlaux, M., Romer, R. L., Mercadier, J., Morlot, C., Marignac, C., & Cuney, M. (2018). 40 Ma of
875 hydrothermal W mineralization during the Variscan orogenic evolution of the French Massif Central
876 revealed by U-Pb dating of wolframite. Mineralium Deposita, 53(1), 21-51.
877 https://doi.org/10.1007/s00126-017-0721-0
878 Hazen, R. M., & Wones, D. R. (1972). The effect of cation substitutions on the physical properties of
879 trioctahedral micas. American Mineralogist: 57(1-2), 103-129.
880 Iiyama, J. T., & Volfinger, M. (1976). A model for trace-element distribution in silicate structures.
881 Mineralogical Magazine, 40(314), 555-564. https://doi.org/10.1180/minmag.1976.040.314.02
882 Keppler, H., & Wyllie, P. J. (1991). Partitioning of Cu, Sn, Mo, W, U, and Th between melt and aqueous fluid
883 in the systems haplogranite-H 2 O− HCl and haplogranite-H 2 O− HF. Contributions to Mineralogy and
884 Petrology, 109(2), 139-150. https://doi.org/10.1007/BF00306474
885 Legros, H., Marignac, C., Mercadier, J., Cuney, M., Richard, A., Wang, R. C., ... & Lespinasse, M. Y. (2016).
886 Detailed paragenesis and Li-mica compositions as recorders of the magmatic-hydrothermal evolution of the
887 Maoping W-Sn deposit (Jiangxi, China). Lithos, 264, 108-124. https://doi.org/10.1016/j.lithos.2016.08.022
888 Legros, H., Marignac, C., Tabary, T., Mercadier, J., Richard, A., Cuney, M., ... & Lespinasse, M. Y. (2018). The
889 ore-forming magmatic-hydrothermal system of the Piaotang W-Sn deposit (Jiangxi, China) as seen from Li-
890 mica geochemistry. American Mineralogist, 103(1), 39-54. https://doi.org/10.2138/am-2018-6196
891 Legros, H., Harlaux, M., Mercadier, J., Romer, R. L., Poujol, M., Camacho, A., ... & Lespinasse, M. Y. (2020).
892 The world-class Nanling metallogenic belt (Jiangxi, China): W and Sn deposition at 160 Ma followed by 30
893 my of hydrothermal metal redistribution. Ore Geology Reviews, 117, 103302.
894 https://doi.org/10.1016/j.oregeorev.2019.103302

Li, J., Huang, X. L., He, P. L., Li, W. X., Yu, Y., & Chen, L. L. (2015). In situ analyses of micas in the Yashan granite, South China: Constraints on magmatic and hydrothermal evolutions of W and Ta–Nb bearing granites. Ore Geology Reviews, 65, 793-810. https://doi.org/10.1016/j.oregeorev.2014.09.028

Li, J., Huang, X. L., Wei, G. J., Liu, Y., Ma, J. L., Han, L., & He, P. L. (2018). Lithium isotope fractionation during magmatic differentiation and hydrothermal processes in rare-metal granites. Geochimica et Cosmochimica Acta, 240, 64-79. https://doi.org/10.1016/j.gca.2018.08.021

Li, X. Y., Lu, J. J., Zhang, R. Q., Gao, J. F., & Wu, J. W. (2021). Magma evolution leading to veinlet-disseminated tungsten mineralization at the Muguayuan deposit: in-situ analysis of igneous minerals. Ore Geology Reviews, 104406. https://doi.org/10.1016/j.oregeorev.2021.104406

Lin, X., Wang, X., Zhang, B., & Yao, W. (2014). Multivariate analysis of regolith sediment geochemical data from the Jinwozi gold field, north-western China. Journal of Geochemical Exploration, 137, 48-54. https://doi.org/10.1016/j.gexplo.2013.11.006

Linnen, R. L., & Cuney, M. (2005). Granite-related rare-element deposits and experimental constraints on Ta-Nb-W-Sn-Zr-Hf mineralization, in Linnen RL and Samson IM, eds., Rare-element geochemistry and mineral deposits. In Geological Association of Canada, GAC, Short Course.

Michaud, J. A. S., Gumiaux, C., Pichavant, M., Gloaguen, E., & Marcoux, E. (2020). From magmatic to hydrothermal Sn-Li-(Nb-Ta-W) mineralization: the Argemela area (central Portugal). Ore Geology Reviews, 116, 103215. https://doi.org/10.1016/j.oregeorev.2019.103215

Marignac, C., Cuney, M., Cathelineau, M., Lecomte, A., Carocci, E., & Pinto, F. (2020). The Panasqueira Rare Metal Granite Suites and Their Involvement in the Genesis of the World-Class Panasqueira W–Sn–Cu Vein Deposit: A Petrographic, Mineralogical, and Geochemical Study. Minerals, 10(6), 562. https://doi.org/10.3390/min10060562

Monier, G., & Robert, J. L. (1986). Evolution of the miscibility gap between muscovite and biotite solid solutions with increasing lithium content: an experimental study in the system K 2 O-Li 2 O-MgO-FeO-Al 2 O 3-SiO 2-H 2 O-HF at 600 C, 2 kbar P H 2 O: comparison with natural lithium micas. Mineralogical Magazine, 50(358), 641-651. https://doi.org/10.1180/minmag.1986.050.358.09

Monnier, L., Lach, P., Salvi, S., Melleton, J., Bailly, L., Beziat, D., ... & Gouy, S. (2018). Quartz trace-element composition by LA-ICP-MS as proxy for granite differentiation, hydrothermal episodes, and related mineralization: The Beauvoir Granite (Echassières district), France. Lithos, 320, 355-377. https://doi.org/10.1016/j.lithos.2018.09.024

Monnier, L., Salvi, S., Melleton, J., Bailly, L., Béziat, D., de Parseval, P., ... & Lach, P. (2019). Multiple Generations of Wolframite Mineralization in the Echassieres District (Massif Central, France). Minerals, 9(10), 637. https://doi.org/10.3390/min9100637.

Monnier, L., Salvi, S., Jourdan, V., Sall, S., Bailly, L., Melleton, J., & Béziat, D. (2020). Contrasting fluid behavior during two styles of greisen alteration leading to distinct wolframite mineralizations: the Echassières district (Massif Central, France). Ore Geology Reviews, 103648. https://doi.org/10.1016/j.oregeorev.2020.103648

Nash, W. P., & Crecraft, H. R. (1985). Partition coefficients for trace elements in silicic magmas. Geochimica et cosmochimica acta, 49(11), 2309-2322. https://doi.org/10.1016/0016-7037(85)90231-5

Neves, L. J. (1997). Trace element content and partitioning between biotite and muscovite of granitic rocks: a study in the Viseu region (Central Portugal). European Journal of Mineralogy, 849-858.

Raimbault, L., Cuney, M., Azencott, C., Duthou, J. L., & Joron, J. L. (1995). Geochemical evidence for a multistage magmatic genesis of Ta-Sn-Li mineralization in the granite at Beauvoir, French Massif Central. Economic Geology, 90(3), 548-576. https://doi.org/10.2113/gsecongeo.90.3.548

Shi, R., Zhao, J., Evans, N. J., Qin, K., Wang, F., Li, Z., ... & Li, X. (2021). Temporal-spatial variations in Li-Fe mica compositions from the Weilasituo Sn-polymetallic deposit (NE China): implications for deposit-scale fluid evolution. Ore Geology Reviews, 104132. https://doi.org/10.1016/j.oregeorev.2021.104132

Schmidt, C., Romer, R. L., Wohlgemuth-Ueberwasser, C. C., & Appelt, O. (2020). Partitioning of Sn and W between granitic melt and aqueous fluid. Ore geology reviews, 117, 103263. https://doi.org/10.1016/j.oregeorev.2019.103263

Schulz, B. (2009). EMP-monazite age controls on PT paths of garnet metapelites in the Variscan inverted metamorphic sequence of La Sioule, French Massif Central. Bulletin de la Société Géologique de France, 180(3), 271-282. https://doi.org/10.2113/gssgfbull.180.3.271

Sokal, R. R., Michener, C. D. (1958). A Statistical Method for Evaluating Systematic Relationships. The University of Kansas Science Bulletin. 38, 1409–38.

Stepanov, A., Mavrogenes, J. A., Meffre, S., & Davidson, P. (2014). The key role of mica during igneous concentration of tantalum. Contributions to Mineralogy and Petrology, 167(6), 1009. https://doi.org/10.1007/s00410-014-1009-3

Sun, K., Chen, B., & Deng, J. (2019). Biotite in highly evolved granites from the Shimensi W–Cu–Mo polymetallic ore deposit, China: Insights into magma source and evolution. Lithos, 350, 105245. https://doi.org/10.1016/j.lithos.2019.105245

Thompson, R. N., Velde, D., Leat, P. T., Morrison, M. A., Mitchell, J. G., Dickin, A. P., & Gibson, S. A. (1997). Oligocene lamproite containing an Al-poor, Ti-rich biotite, Middle Park, northwest Colorado, USA. Mineralogical Magazine, 61(407), 557-572. https://doi.org/10.1180/minmag.1997.061.407.08

Tichomirowa, M., Kässner, A., Sperner, B., Lapp, M., Leonhardt, D., Linnemann, U., ... & Sergeev, S. (2019). Dating multiply overprinted granites: The effect of protracted magmatism and fluid flow on dating systems (zircon U-Pb: SHRIMP/SIMS, LA-ICP-MS, CA-ID-TIMS; and Rb–Sr, Ar–Ar)–Granites from the Western Erzgebirge (Bohemian Massif, Germany). Chemical Geology, 519, 11-38. https://doi.org/10.1016/j.chemgeo.2019.04.024

Tischendorf, G., Förster, H. J., & Gottesmann, B. (2001). Minor-and trace-element composition of trioctahedral micas: a review. Mineralogical Magazine, 65(2), 249-276. https://doi.org/10.1180/002646101550244

Wang, R. (1988).In french. Etude mineralogique et cristallochimique de cassiterite, niobo-tantalates et mineraux dissemines du granite de beauvoir (allier): implications metallogeniques (Doctoral dissertation, Toulouse 3).

Wei, B., Wang, C. Y., Zhao, Z., & Bao, H. (2020). Columbite-group minerals and mica of peraluminous granite record the magmatic-hydrothermal processes that formed the Zhaojinggou TaNb deposit in the North China Craton. Lithos, 370, 105648. https://doi.org/10.1016/j.lithos.2020.105648

Wu, C. M., & Chen, H. X. (2015). Revised Ti-in-biotite geothermometer for ilmenite-or rutile-bearing crustal metapelites. Science Bulletin, 60(1), 116-121. https://doi.org/10.1007/s11434-014-0674-y

975 Xie, L., Wang, R. C., Groat, L. A., Zhu, J. C., Huang, F. F., & Cempírek, J. (2015). A combined EMPA and LA-
976 ICP-MS study of Li-bearing mica and Sn–Ti oxide minerals from the Qiguling topaz rhyolite (Qitianling
977 District, China): The role of fluorine in origin of tin mineralization. Ore Geology Reviews, 65, 779-792.
978 https://doi.org/10.1016/j.oregeorev.2014.08.013
979 Xie, L., Liu, Y., Wang, R., Hu, H., Che, X., & Xiang, L. (2019). Li–Nb–Ta mineralization in the Jurassic Yifeng
980 granite-aplite intrusion within the Neoproterozoic Jiuling batholith, south China: A fluid-rich and quenching
981 ore-forming process. Journal of Asian Earth Sciences, 185, 104047.
982 https://doi.org/10.1016/j.jseaes.2019.104047
983 Xie, L., Tao, X., Wang, R., Wu, F., Liu, C., Liu, X., ... & Zhang, R. (2020). Highly fractionated leucogranites in
984 the eastern Himalayan Cuonadong dome and related magmatic Be–Nb–Ta and hydrothermal Be–W–Sn
985 mineralization. Lithos, 354, 105286.
986 https://doi.org/10.1016/j.lithos.2019.105286
987 Yang, Z., Wang, R., Che, X., Yin, R., Xie, L., & Hu, H. (2020). Formation of columbite and microlite after
988 alteration of Nb-and Ta-bearing biotite from the Lizaizhai pegmatite (Guangning ore district, Guangdong,
989 South China): Identification of a new potential Nb–Ta mineralization type. Journal of Asian Earth Sciences,
990 190, 104154. https://doi.org/10.1016/j.jseaes.2019.104154
991 Yin, R., Han, L., Huang, X. L., Li, J., Li, W. X., & CHen, L. L. (2019). Textural and chemical variations of micas as
992 indicators for tungsten mineralization: Evidence from highly evolved granites in the Dahutang tungsten
993 deposit, South China. American Mineralogist: Journal of Earth and Planetary Materials, 104(7), 949-965.
994 https://doi.org/10.2138/am-2019-6796
995 Zajacz, Z., Halter, W. E., Pettke, T., & Guillong, M. (2008). Determination of fluid/melt partition coefficients
996 by LA-ICPMS analysis of co-existing fluid and silicate melt inclusions: Controls on element partitioning.
997 Geochimica et Cosmochimica Acta, 72(8), 2169-2197. https://doi.org/10.1016/j.gca.2008.01.034
998 Zhang, R., Lehmann, B., Seltmann, R., Sun, W., & Li, C. (2017). Cassiterite U-Pb geochronology constrains
999 magmatic-hydrothermal evolution in complex evolved granite systems: The classic Erzgebirge tin province
1000 (Saxony and Bohemia). Geology, 45(12), 1095-1098. https://doi.org/10.1130/G39634.1

Zhu, Z., Wang, R., Marignac, C., Cuney, M., Mercadier, J., Che, X., & Lespinasse, M. Y. (2018). A new style of rare metal granite with Nb-rich mica: The Early Cretaceous Huangshan rare-metal granite suite, northeast Jiangxi Province, southeast China. American Mineralogist: Journal of Earth and Planetary Materials, 103(10), 1530-1544. https://doi.org/10.2138/am-2018-6511

Zoheir, B., Lehmann, B., Emam, A., Radwan, A., Zhang, R., Bain, W. M., ... & Nolte, N. (2020). Extreme fractionation and magmatic–hydrothermal transition in the formation of the Abu Dabbab rare-metal granite, Eastern Desert, Egypt. Lithos, 352, 105329. https://doi.org/10.1016/j.lithos.2019.105329